

Examining Entropic Unbalanced Optimal Transport and Sinkhorn Divergences for Spatial Forecast Verification

Jacob J. M. Francis^{1,2} | Colin J. Cotter² | Marion P. Mittermaier³

¹NERC Doctoral Training Programme in Science and Solutions for a Changing Planet, Imperial College London, London, SW7 2AZ, UK

²Department of Mathematics, Imperial College London, London, SW7 2AZ, UK

³Met Office, Exeter, Devon, EX1 3PB, UK

Correspondence

Email: jacob.francis18@imperial.ac.uk

Funding information

This work was supported by the Natural Environment Research Council [grant number NE/S007415/1] and the CASE Studentship "Transport methods for the verification of Numerical Weather Prediction (NWP) forecasts" at the Met Office

An optimal transport (OT) problem seeks to find the cheapest mapping between two distributions with equal total density, given the cost of transporting density from one place to another. Unbalanced OT allows for different total density in each distribution. This is the typical setting for precipitation forecast and observation data, when considering the densities as accumulated rainfall, or intensity. True OT problems are computationally expensive, however through entropic regularisation it is possible to obtain an approximation maintaining many of the underlying attributes of the true problem. In this work, entropic unbalanced OT and its associated Sinkhorn divergence are examined as a spatial forecast verification method for precipitation data. It offers many attractive features, such as morphing one field into another, defining a distance between fields and providing feature based optimal assignment. This method joins the growing research by the Spatial Forecast Verification Methods Inter-Comparison Project (ICP) which aims to unite spatial verification approaches. After testing this methodology's behaviour on the Meso-VICTs binary idealised cases, and the ICP's perturbed and Spring 2005 test sets, it is found that the Sinkhorn divergence is robust against the common double penalty problem (a form of phase error), aligns with expert assessments of model performance, and allows for a variety of novel pictorial illustrations of error. It provides informative summary scores, and has few limitations to its application. Combined, these findings place unbalanced entropy regularised optimal transport and the Sinkhorn divergence as an informative method which follows geometric intuition.

KEYWORDS

Optimal Transport, [Sinkhorn Divergence](#), Forecast Verification, [Spatial Method](#), ICP, MesoVICT, Unbalanced Optimal Transport

1 | INTRODUCTION

Without forecast verification, it would be impossible to accurately assess a precipitation, or more generally a Numerical Weather Prediction (NWP), model's overall *goodness*. As observed by [Murphy \(1993\)](#), there are three key factors that contribute to this assessment: consistency, quality, and value. Since Murphy's essay, there have been significant developments in the accuracy of weather models over longer time periods and in their increased spatial resolution. However, as forecasters move to higher resolution models, traditional metrics of quality have struggled to capture the improvements in model accuracy which are believed to be present ([Mass et al., 2002](#)). This development has been coupled with more readily available observational data, spatial and temporal ([Hou et al., 2014](#)). Though, this expansion in data has complicated the determination of quality. While the value of a precipitation forecast is subjective to the user, quality should be objectively quantified, either numerically, graphically, or pictorially, to show the correspondence between the forecast and the observation.

It has been observed that traditional metrics, based on point-wise evaluations, fail to accurately score increasingly complex data ([Brown et al., 2011](#)). One significant complication is the *double-penalty problem*; in this scenario, a forecast predicts the correct spatial extent (shape) and intensity but in the wrong location. Point-wise, or *local*-metrics, penalise this forecast twice – once for failing to detect the correct event and once for predicting an event where there was none. Despite this, local-metrics have undergone many years of research and are a foundation of operational forecasting, meaning that users are often more familiar with reading and interpreting their outputs. What is missing from these local metrics is the consideration of spatial relationships. The emphasis in modern precipitation verification now lies in incorporating this spatial information for greater diagnostic capacity. To maximise impact, this needs to be combined with education around these novel metrics. This will enable users to utilise them in a meaningful and streamlined way.

To address the double penalty problem and incorporate non-local information, such as spatial patterns, structure, and covariance, verification practitioners have researched spatial forecast verification methods under the ICP (Spatial Forecast Verification Inter-comparison Project, [Gilleland et al. \(2009, 2010\)](#)). This collective effort led to the rigorous study, creation, and adaptation of many spatial methods, often leveraging principles from computer vision and image processing in a new guise. From this work and [Dorninger et al. \(2018\)](#), five overarching categories were established, broadly encompassing most identified methods (which are not limited to precipitation verification). These are¹: (i) *distance metrics*, such as Centroid Distance (CDST), Baddeley's Distance (BDEL), and Mean Error Distance (MED) ([Gilleland et al., 2020](#)); (ii) *neighbourhood methods*, including Fraction Skill Score and others as reviewed by [Ebert \(2008\)](#); (iii) *scale separation schemes*, such as intensity-scale techniques using Fourier or wavelet decomposition ([Casati et al., 2004](#)); (iv) *feature-based methods* for example, the Method for Object-based Diagnostic Evaluation (MODE) ([Davis et al., 2006, 2009](#)) and Structure, Amplitude, and Location (SAL) ([Wernli et al., 2008](#)); and (v) *field deformation techniques* like Optical Flow (OF) ([Keil and Craig, 2007, 2009](#); [Marzban and Sandgathe, 2010](#)). Through the ICPs combined effort there is now centralised resources for metrics, their references ([Eric Gilleland, n.d.](#)), their implementation ([Gilleland, 2011](#)), as well as datasets for testing any novel methodologies ([NCAR, n.d.](#)).

This present work shall introduce entropy regularised unbalanced optimal transport (UOT) and its unbalanced Sinkhorn divergence (S_e) counterpart as alternative spatial forecast verification methods and metrics. These approaches draw on recent advances in computer vision and machine learning, and are rooted in rigorous mathematical concepts, including the related Wasserstein distance, balanced and partial optimal transport and the Gaussian Hellinger-Kantorovich distance ([Peyré and Cuturi, 2019](#); [Marzban and Sandgathe, 2010](#); [Séjourné et al., 2019](#); [Liero et al., 2016](#)). In addition, the UOT methodology allows for the calculation of 1) a unit-preserving distance, 2) an approximate transport plan with illustrative vectors, 3) a tunable parameter that defines the scale of relation between features. Taken together, this means that rather than fitting into one of the five above categories of [Dorninger et al.](#)

¹Table 1 of [Gilleland et al. \(2009\)](#) presents a more complete picture, though an update-to-date and full reference to all ICP publications is available at [Eric Gilleland \(n.d.\)](#)

(2018), UOT methodology can bridge multiple categories. Evidence of this is apparent, as in certain scenarios there is a strong link between optimal transport (OT) and optical flow (OF) methods, where both find an optimal morphing between two densities. Equally, as shall be seen through the ICP idealised cases, UOT inherently matches features and those that are separated too far will not be matched: this then mimics a feature based approach. Similarly, the raw cost is unit preserving and hence a suitable distance metric. Additionally, there is the potential, through numerical efficiency considerations, to capture information at sequentially finer scales, imitating a neighbourhood method.

By no means is this the first application of OT or the Wasserstein distance in meteorology. These concepts have been applied in data assimilation (Liu and Frank, 2022; Bocquet et al., 2024; Feyeux et al., 2018), wind speed model aggregation (Papayiannis et al., 2018), hydrological misfit functions (Magyar and Sambridge, 2023), and as a pollutant metric (Farchi et al., 2016; Vanderbecken et al., 2023; Hyun et al., 2022). More pressingly, Skok (2023); Skok and Lledó (2024); Nishizawa (2024) used OT theory as a metric for precipitation data in some capacity. These studies range from testing 1D cases where the precise Wasserstein problem is simple to solve, to more complex 2D fields utilising both static and dynamic OT. In fact, Nishizawa (2024) studied the same entropy regularised UOT object as investigated in the present work, and Skok (2023) introduced a related random-nearest neighbour OT type verification methodology. However, to the best of our knowledge, none have considered the bias effect of the entropic regularisation, or focussed on UOT's use as a metric in its own right.

Specifically, through this investigation the following questions shall be answered:

1. How does UOT behave in the context of the double penalty problem? Is there a diagnostic advantage in using the Sinkhorn Divergence?
2. How does UOT perform geometrically? Can it handle object rotations, detect zero-points and boundaries, or determine whether one field is a subset of another?
3. Can the score alone be diagnostic of translation error, spatial bias and intensity imbalances? Are additional tools such as visualisations of the transport vectors and the marginals necessary for diagnosis of error, or are these a useful aid in their own right?
4. Does the tunable reach parameter define a strict skill threshold (or skill scale), and how does it affect the marginals of the returned plan?
5. Is there a difference in the diagnostic behaviour for different marginal penalisation of the UOT problem? Does this affect the influence of the tunable parameter and the sensitivity to any imbalance in intensity?
6. Is there a way to preferentially forecast to improve its UOT score, i.e. hedging and increasing overlap?
7. How does UOT perform in extreme, edge or null cases? Is it always defined or are there situations where it is no longer defined?
8. Given real intensity data, are any properties from the simplified setting retained or lost? Additionally, is UOT robust to noisy data?
9. Does the spatial metric achieve better alignment with human subjective evaluation, compared to traditional local metrics?

The rest of this article is organised as follows. In Section 1.1 a brief introduction to the background of OT is given (those familiar with the concept may wish to skip this). In Section 2 the data is introduced, including the ICP's binary idealised cases in Section 2.1, as well as real textured intensity cases in Section 2.2. Section 3 then presents the methodology of UOT_ϵ and S_ϵ , with a brief note on implementation in Section 3.2. Then, Section 4 confers the first results for the simple set of idealised cases, before testing the scattered, noisy and edges cases in Sections 4.1.7 and 4.1.8. Real textured intensity are then tested in Section 4.2. Finally, Section 5 presents a summary and outlook (Section 5.1).

1.1 | Optimal Transport

Optimal transport (OT) was originally devised by [Monge \(1781\)](#) as a logistics problem, with the goal of optimising the construction of wartime trenches. From its inception, to economic interpretation and development by [Kantorovitch \(1958\)](#), and to its more recent boom in research and application in machine learning due to [Cuturi \(2013\)](#)'s regularised version, OT has found use in a vast array of fields, from computer vision, machine learning and signal processing to fluid dynamics, economics, biology, and, more recently, spatial forecast verification ([Santambrogio, 2015](#); [Benamou and Brenier, 1998](#); [Kolouri et al., 2017](#); [Gramfort A et al., 2015](#); [Skok, 2022](#)).

By definition, an OT problem aims to find a minimising map between two density distributions, provided with a cost of transporting density from one place to another. In the meteorological context this could be any quantity described as an intensity, e.g. accumulated rainfall. Mathematically and computationally, the space of possible maps to minimise over is unwieldy, and progress is made by relaxing the condition that the mapping is one-to-one. Instead of mass transporting from just one point to another, now mass from any point is allowed to be split and distributed to many points.

This relaxation is known as Kantorovich's (balanced) OT problem and is defined as follows (for full details starting from Monge's formulation, see [Villani \(2009\)](#)). Given two fields, which are represented by discrete data $\{\alpha_i\}_{i=1}^N, \{\beta_j\}_{j=1}^M$ on grids $x_i \in \mathcal{X} \subset \mathbb{R}^2$ and $y_j \in \mathcal{Y} \subset \mathbb{R}^2$ which do not necessarily have to be the same grid. The density is constructed as $\alpha = \sum_i \alpha_i \delta_{x_i}, \beta = \sum_j \beta_j \delta_{y_j}$, with the condition (for balanced OT) that $\sum_i \alpha_i = \sum_j \beta_j = 1$. Notationally, δ_{x_i} allows us to define a grid through summations, and $\alpha_i \delta_{x_i}$ says there is weight α_i at grid point x_i . The Kantorovich balanced OT problem searches for an optimal joint density, $\pi = \sum_{i,j} \pi_{i,j} \delta_{x_i} \delta_{y_j}$, such that it has left marginal equal to α and right marginal equal to β , i.e. $\pi_{1,j} := \sum_i \pi_{i,j} = \beta_j, \pi_{0,i} := \sum_j \pi_{i,j} = \alpha_i$. The transport plan $\pi_{i,j}$ tells us how much mass is transported from x_i to y_j , allowing for the mass in x_i to be split and transported to multiple points. The transport plan is optimal if it minimises the associated cost or energy,

$$\sum_{i,j} c_{i,j} \pi_{i,j}. \quad (1)$$

Here $c_{i,j} = c(x_i, y_j)$ for some function c which defines a cost. This cost function should characterise the cost of moving mass from point $x_j \in \mathcal{X}$ to $y_j \in \mathcal{Y}$. In the setting of precipitation data, the 'mass' is considered as accumulated rain volume, or intensity, for a given mesh-point or region, i.e. the weights α_i, β_j . If the cost is chosen as an L_p -norm (defined via $\|X\|_p = (\sum_i (x_i)^p)^{\frac{1}{p}}$), then this is known to define Wasserstein's p-distance ([Peyré and Cuturi, 2019](#)). For precipitation data, let us define the cost of moving a certain volume of rain via the squared Euclidean norm or L2-norm with a factor of 1/2 so that transport vectors align with Barycentres (Section 3.1.1). That is, the cost function throughout shall be defined as $c(x, y) = \frac{1}{2} \|x - y\|_2^2$.

In the 1D setting, solving (1) becomes a simple sorting problem. However, in 2D solving the true Wasserstein distance is non-trivial. For instance, given discrete densities the cost, $c_{i,j}$, defines a matrix, and the associated optimisation problem is a linear program. Subsequently, it suffers from the *curse of dimensionality*. Solving this problem becomes inhibitive for a hundred or so points. Yet for NWP data, grids typically consist of many of thousands of points, even into the millions.

To overcome this dimensionality problem, [Cuturi \(2013\)](#) proposed a further relaxation, known as *entropic regularisation*. This regularisation corresponds to the inclusion of entropy, or a Kullback-Leiber (KL) penalty term between some reference and the plan, which we shall describe below. It has received much interest and has been shown to be capable of scaling to millions of points on modern GPU hardware ([Feydy et al., 2019](#); [Feydy and Roussillon](#)). Beneficially, whilst any relaxation of a problem will introduce error, the error (or *bias*) in entropic regularisation has a known *debiased* counterpart ([Feydy et al., 2019](#)). This error-corrected formulation of OT is known as the Sinkhorn divergence (S_ε). It requires the computation of two extra terms whose additional calculation cost is minimal and capable of being solved in parallel to the main computation.

Unfortunately, to the detriment of application to real forecast-observation pairs, the definition given in (1) assumes the two input densities have equal total mass (hence the term "balanced OT"). That is to say, it is assumed that the two fields are unbiased ($\sum_i \alpha_i = \sum_j \beta_j$). This is generally an unrealistic situation and so prevents the use of real rain volumes and intensities (or spatial coverage). One solution to this is to scale the forecast and observation fields to have the same total mass. This is then similar to the idea of applying a percentile threshold which effectively removes the bias, something that has often been used to address bias, e.g. (Mittermaier et al., 2013). However, this will lead to a loss of information: a model could be significantly overforecasting intensities, which is undetected if the volumes are forced to be equal. Instead, to overcome this issue and not lose information, a further relaxation to the optimisation is introduced. This generalised problem corresponds to the static formulation of unbalanced optimal transport (UOT, Liero et al. (2016)) (as opposed to the dynamic (unbalanced) formulation of Benamou and Brenier (2000)). In this setting, the input fields are allowed to have different total masses and the returned marginals (which relate to the forecast and observed fields) of the optimal plan should be *close* to but not exactly equal to the input fields. Additionally, the definition of *close* is open to choice, provided it follows a suitable divergence (see Séjourné et al. (2019) for details). UOT then compares two fields by a combination of transport and pointwise modification of the marginals.

In this work two penalisations are investigated; Kullback-Leiber (KL) divergence and total variation (TV). These are defined given discrete densities $\lambda = \sum_k \lambda_k \delta_{z_k}$, $\gamma = \sum_k \gamma_k \delta_{z_k}$, for some grid points z_k and where if $\gamma_k = 0$ then $\lambda_k = 0$, as

$$KL(\lambda|\gamma) := \sum_k \lambda_k (\log(\frac{\lambda_k}{\gamma_k}) - 1) + \sum_k \gamma_k, \quad (2)$$

$$TV(\lambda|\gamma) := \sum_k |\frac{\lambda_k}{\gamma_k} - 1| \gamma_k, \quad (3)$$

recalling that $\lim_{x \rightarrow 0} x \log(x) = 0$. These divergences blow-up for negative weights, enforcing positivity by construction.

By directly viewing marginals of π or calculating the error between the input and marginal, various diagnostic capabilities can be identified. These diagnostics can then be linked to a reach parameter, resembling a skill-scale parameter, which we discuss later. Taking this further, united under the same framework of OT are an array of tools. For instance, through the joint probability plan it is possible to calculate an approximate map from the observation to the forecast and *vice versa*. In a similar fashion to OF, these are not one-to-one correspondences and different information is gained from one versus the other. Once these transport vectors have been uncovered, it is possible to calculate average statistics, such as average direction and magnitude of transport, or to consider the distribution as a whole. This form of information is considered in the precipitation attribution distance (PAD) methodology (Skok, 2023). It is clear that the UOT framework offers a range of diagnostic strategies. Rather than just point-wise considerations being evaluated and averaged, the underlying optimisation is taking into account spatial information and the effort to move rain volumes within the domain.

Throughout this work, no specific comparator metric is selected, though it is worth noting some similarities that OT holds with other metrics. In particular, we consider differences with OF methods, since OT can also be considered a morphing technique. In terms of their respective implementations, the LK-OF method (Lucas and Kanade, 1981) relies on the underlying assumptions that the fields are continuous as local spatial derivatives are taken, and that changes in derivatives are small between the two fields. These assumptions are not always true and are not required for OT. Marzban and Sandgathe (2010) extend the LK-OF method by including higher-order terms in the Taylor expansion, creating a nonlinear optimisation problem that they tackle through the BFGS algorithm, which has a per-iteration complexity of $O(n^2)$ (n being the number of grid points). Alternatively, Keil and Craig (2007) consider displacement vectors found through pyramidal matching. There is no explicit complexity for this method and would go beyond the

scope of this work, however the pyramid matching itself has complexity $O(nL)$ (Grauman and Darrell, 2005) (where L in the number of layers in the pyramid), then Keil and Craig (2007)'s method searches each layer for an optimal local matching. This process is similar to solving the Earth Mover's Distance, a related optimal transport problem, though without entropic regularisation. Both OF methods have one tunable parameter which defines the window in which to look for perturbations, or the number of layers in the pyramid coarse-fine graining. Entropy regularised UOT has a complexity of $O(n^2 \log n)$ (provided the entropic parameter is suitably chosen depending on the number of grid points and desired convergence criteria), and has one tunable parameter relating to locality (Berman, 2020; Mériçot and Thibert, 2020). However, unlike the LK-OF method, which handles non-matches through local squared errors, UOT allows for the destruction of mass when no match is possible or when matches are too distant.

2 | DATA SET DESCRIPTION

In this investigation, we examine UOT's behaviour through the binary geometric test cases of Gilleland et al. (2020), and the perturbed and Spring 2005 sets of Ahijevych et al. (2009); Kain et al. (2008). Ahijevych et al. (2009) also discusses idealised two-step-intensity cases, which are covered in Nishizawa (2024). Additionally, rather than investigating the test cases in chronological order of the studies, first the simple binary cases are examined, before looking at the inclusion of intensity and concluding with the real textured precipitation forecasts. In this way results are built up from the most simple cases.

2.1 | ICP Binary Geometric Cases

The idealised geometric binary test cases were created by Gilleland et al. (2020), under the MesoVICT project (Mesoscale Verification Intercomparison over Complex Terrain). In the preliminary study, distance metrics were tested against various combinations of the 50 plus cases which make up the test set. The authors created the cases to test different behaviours, such as: hits and misses, the double penalty problem, spatial biases in a model, and edge and extreme cases. The chosen shapes are intended to replicate typical fields found over more complex terrain and at higher resolution, under a thresholding strategy. This is where an event is defined as being above some threshold of precipitation or in a certain quantile of that forecast, then assigned one or zero for the event occurred, or not. In this fashion, only the shape within the domain changes, not the intensities. The benefit of studying these binary cases first is to distinguish amplitude (or intensity) errors from transport and shape or extent (e.g. spatial) errors.

The binary cases lie on a 200 by 200 regular grid, with no underlying physical units. Since UOT operates in density space, it has the capacity to squeeze and stretch shapes and thus over- or under-fill grid points from their input intensities. With this in mind, a thresholded interpretation is not wholly appropriate. Instead, these are treated as examples of areal extents changing with, simple, uniform intensity within the shape bounds. The full set of possible cases is illustrated in Figures 2, 3, 5, 7, 9, in Gilleland et al. (2020), where only a subset is considered here — see 1.

2.2 | ICP Intensity Cases

The second set of data probes UOT's behaviour with more realistic textures and intensities, rather than simple shapes with flat intensities. Inherently, UOT operates with densities, therefore the framework remains unchanged. However, the data now carries true units of intensity.

The real textured cases are from Ahijevych et al. (2009), which was the initial comparative study for spatial metrics under the ICP; the MesoVICT sets emerged a decade later. This integral dataset consists of three subsets, (i) two step idealised geometric intensity cases, (ii) a single real forecast over the US where the forecast-observation pairs are synthetic perturbations of the observation, and (iii) real forecast-observation pairs for 3 models in Spring 2005. These

Case	Description
C1	Radius 20 circle, centred at (100, 100) (base case)
C2	C1 centred at (140, 100)
C3	C1 centred at (180, 100)
C4	C1 centred at (140, 140)
C6	Two radius 20 circles centred at (100, 140) and (100, 60)
C7	C6 with lower circle shifted (40, →)
C8	C6 with lower circle shifted (80, →)
C9	Radius 60 circle, centred at (100, 100)
C11	Union of C1, C3 and C4
C12	Two radius 20 circles centred at (120, 160) and (80, 40)
C13	One radius 8 circle centred at (75, 25) and one radius $8/\sqrt{2}$ centred at (88, 180)
C14	C13 with upper circle shifted (25, →) and lower circle shifted (50, →) (mimicking mirroring in $x=100$)
E1	Vertical large ellipse
E2	E1 at 45°
E3	E1 at 90°
E4	E1 at 135°
E6	Small ellipse at 45° angle
E7	Small horizontal ellipse
E9	E1 shifted (25, →)
E10	E2 shifted (15, →) and (20, ↓)
E11	E3 shifted (25, ↓)

Case	Description
E12	E4 shifted (15, →) and (20, ↑)
E14	E6 shifted (8, ↓) and (10, ↑)
E19	Three vertical ovals centred at (100, 40), (100, 55), and (125, 75), scaled by (40, 5), (35, 5), and (25, 5), respectively
E20	E19 smoothed using a disk kernel with radius 12
H1	Compliment of C1
H2	Compliment of C2
P2	Full field, all ones.
P3	One point at (1, 1)
P4	One point at (200, 200)
P5	One point at (100, 100)
P6	Four points in the four corners
P7	Four points near the middle of each boundary at (1, 100), (100, 1), (200, 100) and (100, 200)
N1	C1, but with 0.1% frequency randomly generated noise
N2	C4, but with 0.1% frequency randomly generated noise
N3	Union of C4 and P5
N4	Union of C4 and P3
S1	Scattered events (frequency 5%) inside a circular envelope with radius 35 centred at (50, 100)
S2	As in S1, but a different realisation
S3	As in S1 and S2, but with the envelope shifted (100, →) and a different realisation

TABLE 1 Table of idealised cases discussed in this report. For full description of all possible cases, see [Gilleland et al. \(2020\)](#). The domain is in a 200 by 200 grid, indexing from (1,1) to (200,200), using coordinates (horizontal, vertical). For the ellipse cases, the ratio of the major vs minor axis is 5:1 with dimensions of the ellipses either 100 by 20 (large ellipse) or 25 by 5 (small ellipse). All ellipses are centred at (100, 100) unless translated. Notation; C circles, E ellipses, P points, S scattered, N noisy and H hole cases.

shall be referred to as the geometric intensity cases, fake perturbed cases, and the Spring 2005 cases, respectively. However, as mentioned, analysis of the geometric intensity cases, (i), is not repeated here.

All three datasets use the same 4km grid with size 601 by 501 (501 in Latitude, 601 in Longitude), where the real data corresponds to forecasts over the Rockies during Spring 2005. For our exploratory investigation, the fields are placed on a regular uniform grid of the same size, i.e. a 605 by 501 box, rather than the true latitude-longitude grid. This allows a more principled examination of the methodology and a true distinction of grid effects. Since OT allows for two different meshes to be compared, grid effects and imperviousness to the grids themselves will be explored in future work.

For a full description of the perturbed cases, consult Table 2 in [Marzban et al. \(2009\)](#) and there-in. In brief, the observation is one realisation (fake000), then forecasts fake001-005 start with a 5 point shift south and 3 point shift east, where sequential cases double in both directions. fake006 and fake007 are at the same location as fake003, but with 1.5 times (multiplicative) the intensity of fake001, and minus 0.05 inch (1.27 mm) (additive) the intensity. Importantly, all these cases are not balanced, because points shifted out of the domain are removed and new points set to zero.

Lastly, the Spring 2005 cases consist of predictions from three models plus observations (stage II precipitation analysis) ([Lin and Mitchell, 2005](#)). The models are wrf4ncar, wrf4ncep, and wrf2caps, which are run at 4km, 4km and 2km respectively. They are then interpolated to the courser resolution 4km grid. Experts were asked to subjectively score the models for each valid time. Here, as in [Keil and Craig \(2009\)](#), 9 time stamps are presented and the authors' Table 3 is used for the average expert scores. An important finding through [Ahijevych et al. \(2009\)](#) was the lack of alignment between subjective scoring and traditional metrics. In contrast, UOT methodology restores this disassociation with subjective scoring, as shown in Section 4.2.

This thorough testing aims to provide insight into how UOT performs with intensity and real textured rain, assessing its ability to diagnose pure transport alongside unequal weighting of regions of rain. The evaluation seeks to determine how much can be deciphered from the scores, with or without further visualisation. Additionally, the potential to rank models and align these rankings with the subjective scoring from the original ICP work is demonstrated.

Note all data used is available through [NCAR \(n.d.\)](#).

3 | UNBALANCED OPTIMAL TRANSPORT AND SINKHORN DIVERGENCE

To consolidate notation, consider a verifier is given a forecast density $\mu_F = \sum_j \mu_{F,j} \delta_{X_{F,j}}$ and an observation density $\mu_O = \sum_i \mu_{O,i} \delta_{X_{O,i}}$ both representing precipitation over some accumulation period, in some region represented by two grids $X_{O,i} \in \Omega_F \subset \mathbb{R}^2$, $X_{F,j} \in \Omega_O \subset \mathbb{R}^2$. In general, these do not have to be the same grid. The goal is to assess the quality of agreement between these fields, using the machinery of UOT and in two variants. The first variant uses KL relaxation of the marginal mass, the second variant TV (see (3) and (2)). These were picked for their distinct characteristics: TV favours edges, filling the weighting in the nearest support, creating sharp cut-offs. In contrast, KL favours filling all the support smoothly with some mass everywhere, at the expense of over or under distributing mass. For full details of UOT and the associated Sinkhorn divergence, see [Séjourné et al. \(2019\)](#) and [Chizat et al. \(2016\)](#). Here a high level sketch will be given, providing only the necessary points for our methodology. Let us define the UOT problem as

$$\frac{\text{UOT}_\varepsilon(\mu_O, \mu_F | \rho)}{\rho} = \min_{\pi} \underbrace{\sum_{i,j} \left(\frac{\|X_{O,i} - X_{F,j}\|}{\sqrt{2\rho}} \right)^2 \pi_{i,j}}_{\text{regularised transport cost}} + \underbrace{\frac{\varepsilon}{\rho} \text{KL}(\pi | \mu_O \otimes \mu_F) + D(\pi_0 | \mu_O) + D(\pi_1 | \mu_F)}_{\text{marginal error cost}}, \quad (4)$$

where entropic regularisation parameter $\varepsilon > 0$, tunable parameter $\rho > 0$, and where D is either the KL divergence or TV and the left and right marginals are denoted π_0 and π_1 , respectively. The notation $\mu_O \otimes \mu_F$ defines the outer product defined as $(\mu_O \otimes \mu_F)_{ij} = \mu_{O,i} \mu_{F,j}$. The entropic regularisation and marginal penalties enforce desired constraints on $\pi_{i,j}$, such as positivity and feasibility. To solve this minimisation problem, a dual associated problem is found and Sinkhorn's iterative algorithm is used as a fixed-point type update. See Supplementary Materials S1 for more details and references on this.

Notice that changing ρ changes the balance of transport cost and marginal error penalty. That is to say, increasing ρ enforces smaller marginal error, so that the inputs and plan marginals must match more closely. Whilst a smaller parameter permits more error in the marginals, thus greater differences between the input and marginal is allowed. By, writing the unbalanced problem in the manner of equation (4) highlights the distance dependence on the tunable parameter ρ . If two points $X_{O,i}$ and $X_{F,j}$ are too far apart, i.e. the distance between them is greater than $O(\sqrt{2\rho})$, then it is cheaper to pay to destroy mass than to move it. If this is the case $\pi_{i,j}$ is set to zero, which follows from complementary slackness, or close to zero in the regularised setting. On the other hand, if the points are separated by less than this, it is feasible to transport the point and not pay to destroy the associated mass. Séjourné et al. (2019) refer to this relationship in ρ as the *reach*. Hence, let us define the reach as $\sqrt{2\rho}$ with units of distance. These two views of ρ , as a penalty parameter or reach distance, are central and will be drawn upon in Section 4.

By way of an overview, the iterative Sinkhorn optimisation is undertaking the following process; a possible transport joint plan is proposed. Here we use the product of the two inputs which has, by construction, the correct marginals. Starting from the observation marginal (wlog), its error against the true observation is calculated, defined by KL or TV. This error is then mapped through the proposed plan and used to optimise the forecast marginal, and implicitly the plan. Now the forecast marginal and input error is calculated, mapped, and used to update the observation marginal and implicitly the plan, once more. This iterative process is repeated, minimising the transport plan and adapting to the density inputs. By controlling the contributions of each term in (4), through ρ , it is possible to prioritise making the marginal and input densities more similar or prioritise cheaper transport. Again, this highlights the alternative optimisation viewpoint of ρ as a marginal penalty parameter.

3.1 | Sinkhorn Divergence

Through entropic regularisation, transport plans become increasingly diffusive around the true non-entropic plan. This is known as *blurring* of the plan, which is a form of bias. This bias manifests as the transport plan (and transport vectors) being distorted towards centres of mass (Feydy et al., 2019). It also results in $\text{UOT}_\varepsilon(\mu, \mu) \neq 0$ for arbitrary μ . A significant contribution of this work shall be the study of the unbalanced Sinkhorn divergence, a debiased counterpart to the entropy regularised biased problem, as a spatial forecast metric.

In equation (5) the post debiasing technique is introduced, where the *symmetric* debiasing terms remove the associated entropic error up to the next order in ε . Séjourné et al. (2019) define the unbalanced Sinkhorn divergence as

$$S_\varepsilon(\mu_O, \mu_F | \rho) = \text{UOT}_\varepsilon(\mu_O, \mu_F | \rho) - \underbrace{\frac{1}{2} \text{UOT}_\varepsilon(\mu_O, \mu_O | \rho) - \frac{1}{2} \text{UOT}_\varepsilon(\mu_F, \mu_F | \rho)}_{\text{symmetric debiasing terms}} + \underbrace{\frac{\varepsilon}{2} (m(\mu_O) + m(\mu_F))^2}_{\text{mass imbalance term}}, \quad (5)$$

where $m(\cdot)$ measures the total mass of the density. This corrects the transport vectors, and gives provably that $S_\varepsilon(\mu, \mu) = 0$. Since these are post debiasing steps, each UOT_ε problem is solved separately. For efficiency they may be solved in parallel.

3.1.1 | Transport vectors

Alongside the scores (interchangeably the costs) returned from S_ε and UOT_ε , there is the possibility to calculate transport vectors, which are found through the *barycentric projection* using the transport plan. These barycentric projections are approximations to a transport map. They are formed through the joint probability plan, and allow for the creation of transport vectors between the two inputs, since the vector is formed from the vector between an initial point to its mapped counterpart. The definition of the barycentric map is

$$X_{O,i} \in \Omega_O \rightarrow \frac{\sum_j \pi_{i,j} X_{F,i}}{\pi_{0,i}} \in \Omega_F, \quad (6)$$

$$X_{F,j} \in \Omega_F \rightarrow \frac{\sum_i \pi_{i,j} X_{O,i}}{\pi_{1,j}} \in \Omega_O. \quad (7)$$

When the total mass sums to 1, so that $\pi_{i,j}$ defines a discrete joint probability distribution, they correspond to conditional expectations.

As stated, this quantity is not debiased, nor is π able to be debiased through its primal interpretation. However, (Feydy et al., 2019) found that gradient of S_ε is exactly the desired debiased quantity. This provides the debiased barycentric mapping,

$$X_{O,i} \in \Omega_O \rightarrow \frac{\sum_j \pi_{i,j} X_{F,j}}{\pi_{0,i}} - \left(X_{O,i} - \frac{\sum_k \pi_{i,k}^{\text{sym},O} X_{O,k}}{\pi_{0,i}^{\text{sym},O}} \right), \quad (8)$$

$$X_{F,j} \in \Omega_F \rightarrow \frac{\sum_i \pi_{i,j} X_{O,i}}{\pi_{1,j}} - \left(X_{F,j} - \frac{\sum_k \pi_{k,j}^{\text{sym},F} X_{F,k}}{\pi_{1,j}^{\text{sym},F}} \right), \quad (9)$$

where $\pi^{\text{sym},O/F}$ denotes the symmetric plans for solving the problems $\text{UOT}_\varepsilon(\mu_O, \mu_O)$ and $\text{UOT}_\varepsilon(\mu_F, \mu_F)$, respectively. We use the (debiased) barycentric mapping to define transport vectors for each point.

In essence, this describes the underlying transport that is occurring through the plan. Auspiciously, following (Feydy et al., 2019) and by the deliberate choice of the half squared Euclidean cost the gradient of the functional ($\text{UOT}_\varepsilon/S_\varepsilon$) in space corresponds to (debiased) barycentric projection. Given the underlying transport vectors, the mean average transport magnitude and direction (ATM and ATD) is formed via averaging all vectors and calculating its magnitude and direction. Note that if points have zero mass these have undefined transport vectors (division by zero) and are left out of the averaging, and in general are ignored. With this in mind, similarly to the OF based DAS verification methodology of Keil and Craig (2007, 2009), it is possible to calculate the approximate map in both a forward (observation to forecast) and inverse direction. Both of these will be reported, with differences used as a diagnostic tool.

3.2 | Implementation

For more details on the Sinkhorn algorithm and implementation, see Supplementary Materials S1 or (Francis, n.d.) for the Python implementation. For our purposes, it is sufficient to know that $\varepsilon \sim 1/\sqrt{N}$ and is fixed through the grid resolution to maintain convergence (Mérigot and Thibert, 2020). While efficiency was not the primary focus of this work, the Sinkhorn algorithm implementation was accelerated using two straightforward techniques: tensorisation (Remark 4.17 in Peyré and Cuturi (2019)) and ε -annealing (Schmitzer, 2019; Chizat, 2024), which are detailed in Section S1.1. With these optimisations the Sinkhorn algorithm for the ICP binary cases (40,000 points) required an average of 2.21 seconds, while the perturbed and Spring 2005 cases (301,101 points) took on average 36.6 seconds. These were ran on one NVIDIA GeForce RTX 3090 GPU, with a convergence tolerance of 10^{-12} . Note that the runtime depends on the type of penalisation used (e.g., TV regularisation was seen to be typically slower) and the chosen reach

parameter.

Additionally, because physical data often exists on large scales, particularly when dealing with global or large regions at high resolution, certain challenges arise. The underlying algorithm operates in exponential and logarithmic domains, which are generally more stable but can still result in numerical overflows and underflows on such large scales. To mitigate these numerical errors, a scaling is introduced to remove the dimensions of grid length and mass (or total intensity). Specifically, given a domain or region of interest, the typical length scale is defined as L , and the total rain volume (or mass) is defined as M . These dimensions can be reintroduced by simple multiplication of $M^2 \cdot L^2$, or the cost can be left in a dimensionless form.

The length scale, L , is typically straightforward to determine from the grid. However, M may not always be as easily derived; it can be estimated from climatological data for the region or using a climatological average. In this work, the suboptimal in-sample average is utilised, although an out-of-sample value would be preferable for future studies. Throughout, for interpretability reasons and because no actual units are attached, the M scaling is not reintroduced. To recover the actual cost, one would need to multiply the metric costs by M^2 .

This now provides us with a range of different scores to consider: the UOT energy in two flavours (UOT_{ε}^{KL} and UOT_{ε}^{TV}) as well as each of their debiased Sinkhorn divergence counterparts (S_{ε}^{KL} and S_{ε}^{TV}). Similar to the debiased ATM and ATD in the forward and inverse direction (KL/KL^{-1} and TV/TV^{-1}), the error for the bias case is known to be an issue and so the results for the bias transport vectors are not shown (Feydy et al., 2019). Further evidence for this choice is presented in the beginning of 4.1. Below, a few other visualisations are explored, especially for viewing the marginals. These are intended to illustrate the possibilities behind UOT, and demonstrate the capacity of this methodology.

4 | RESULTS AND ANALYSIS

Through-out the proceeding section, recall that the units of intensity are omitted to aid interpretability of the scores. Hence, one may imagine scaling the scores by M^2 if full units are desired. For reference, for the binary cases $L = 200$, and for the textured cases, $L=601$. Any cases which are not presented in the following section but are presented in Gilleland et al. (2020) can be found in Section S1.2 and Section S1.3.

4.1 | ICP Binary Geometric cases

Notationally, comparisons between two fields, e.g. $C1$ and $C2$, are written as $C1C2$ (or fake000fake001 for the intensity cases). This means that $C1$ is treated as the observation field and $C2$ the forecast. For each case the UOT score or costs, in KL and TV flavours, are calculated. Both of these are also considered in their biased ($p=UOT_{\varepsilon}$) and debiased ($se=S_{\varepsilon}$) forms. We write $UOT_{\varepsilon}^{KL/TV}$ and $S_{\varepsilon}^{KL/TV}$, whilst UOT is used when referring to the general methodology. Additionally, the mean average transport magnitude (ATM) and direction (ATD) are reported in both flavours and in the forward (KL/TV) or inverse (KL^{-1}/TV^{-1}) direction, i.e. observation to forecast ($C1 \rightarrow C2$) or vice versa. As a reminder of the cases used in this work, see Table 1. The UOT_{ε} cost (and implicitly S_{ε}) reported throughout is equation (4) multiplied by ρ . For these binary cases $\varepsilon = 0.005 \cdot L^2$, following Mériqot and Thibert (2020). Hence, this is set by the grid structure, not the user. Lastly, recall that the units of the costs presented are in (half) squared Euclidean space. For example, $C1C2$ (Figure 2) has an expected transport cost of 800, which corresponds to a 40-point shift, as $\frac{1}{2} \cdot 40^2 = 800$. This cost is then scaled by the relative total rainfall/areal extent, or mass. The average mass is $M = 1873.5$, and $C1$ has a mass of 1345, so in Figure 2, the cost is $574 \sim 800 \cdot 1345/1873.5$.

4.1.1 | The perfect forecast

A perfect forecast-observation pair, C1C1, is investigated in Figure 3. Here, with two equivalent fields $S_\varepsilon^{KL/TV}$ returns zero, whilst UOT_ε is dominated by entropic error. Following Séjourné et al. (2019), this is expected since S_ε defines a pseudometric, being positive-definite and convex. However, $UOT_\varepsilon^{KL/TV}$ may still prove powerful, especially if constituent terms are considered, hence it shall be demonstrated throughout. For this case, Figure 1 compares the underlying biased and debiased transport vectors where there is a clear correction away the centre of mass from debiasing. As discussed, this is a known property of biased UOT, hence throughout the ATM and ATD are presented with respect to the debiased transport vectors. Notice that, while the magnitudes of the debiased cases are small on average, there may still be some nonzero ATD values returned. However, appropriately, the ATM values remain zero. This is reflected in the results.

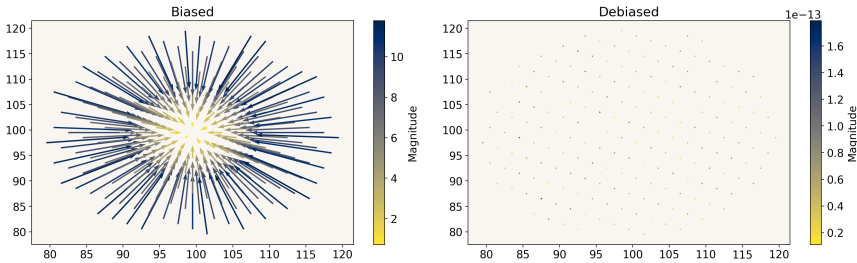


FIGURE 1 Biased vs debiased transport vector illustration with KL marginal penalty for the C1C1 case (cropped to region of interest). The TV flavour similarly suffers from bias. Left: Biased UOT transport vectors, Right: Debiased UOT transport vectors. A regular sample of the vectors are shown to prevent overcrowding. Notice the scale of the magnitude bar for the debiased cases. $\varepsilon = 0.005 \cdot L^2$, $\rho = 1 \cdot L^2$.

4.1.2 | Boundary effects

The next question investigates whether UOT is sensitive to or, influenced by, proximity to the boundary. Do the zero points surrounding an isolated feature change the score? This is explored through C1C2, C2C3 and C2C4: see Figure 2 and Figure 3. Across flavours, all three cases have equal scores and the ATD shows the expected transport direction. Simultaneously, on the regular grid, how orientation affects the score can be examined through C2C3 vs C2C4 and E1E9 vs E2E10: see Figure 2. Again, the pairs at 90° rotation are equal, with the expected ATD. However, the costs for E2E20 are only approximately close to E1E9, although the ATD is correct. This sensitivity is expected since on a regular grid, the fields are no longer equivalent and the number of nonzero points changes. E1E9 has 1553 non-zero points and E2E10 has 1573: the sensitivity comes directly from these different masses. Overall this demonstrates robustness to the boundary, which is not true for all distance metrics (see Baddeley’s metric in Gilleland et al. (2020)), and some sensitivity to rotation on this regular grid, but this is not detrimental so long as the shift remains equivalent.

4.1.3 | Sensitivity to phase error for balance cases

As UOT is being presented as a spatial forecast verification metric, it is paramount that it is capable of diagnosing transport error. Through the cases C1C1, C1C2, C1C5, and C1C3 (in Figure 3), transport and sensitivity to the double penalty problem is scrutinised by comparison to the known Wasserstein-2 ($\frac{1}{2}W_2^2$) distance which corresponds to the balanced, non-entropic version of UOT_ε . In these simple settings it is known to diagnose the transport shift error, finding the shortest path and optimal cost which corresponds to this shift. Indeed, in Figure 3, S_ε is diagnosing close

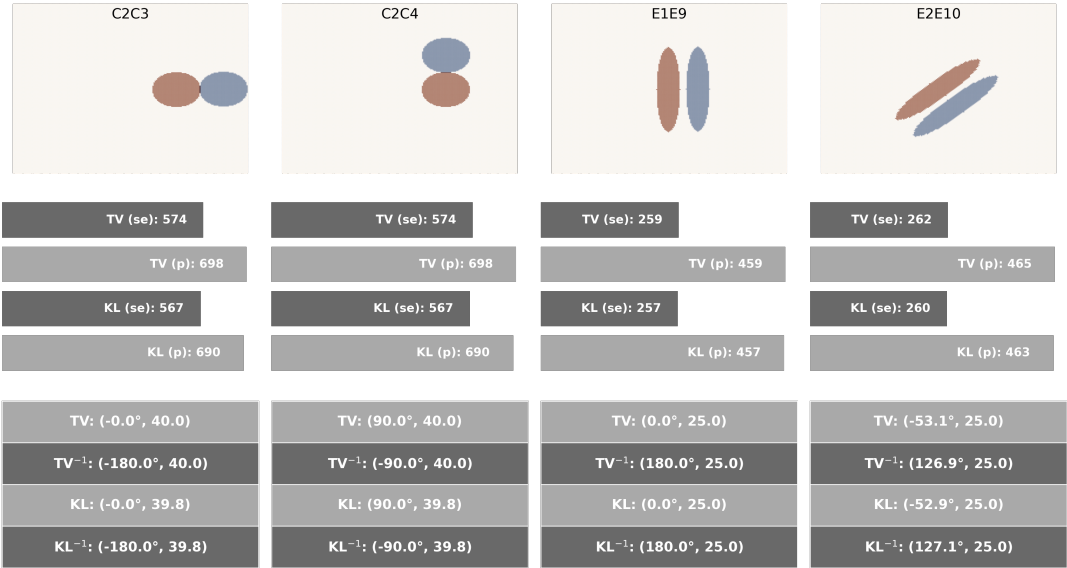


FIGURE 2 Cases illustrating robustness to orientation and rotation of events on a regular grid. Notice that for E2E10 the -53.1 degree ATD (and its inverse) appears from these events being 15 grid points east and 20 south which preserves the correct separation after rotation of the observation. The top four horizontal bars display; S_{ε}^{TV} , UOT_{ε}^{TV} , S_{ε}^{KL} , UOT_{ε}^{KL} . The lower table presents the mean (ATD, ATM) in both flavours, and with the forward and inverse debiased vectors. The red (darker) colour indicates observations, while the blue (lighter) represents forecasts. $\varepsilon = 0.005 \cdot L^2$, $\rho = 1 \cdot L^2$.

to the expected cost (consider the C1C2 case described above), and the ATM is correctly diagnosing the shift. Through the progressive cases, the costs are scaling appropriately following a quadratic relationship to the shift. In summary, it is possible to diagnose pure transport error (or $\frac{1}{2}W_2^2$ cost), and hence not be susceptible to the double penalty problem in the balanced mass setting. This diagnostic capability is closer to $\frac{1}{2}W_2^2$ in the S_{ε}^{TV} than S_{ε}^{KL} , though it will be shown to be ρ and mass-balance dependent.

To test this further, a constructed set of balanced transport cases at 10 grid point shift increments² is created. Their S_{ε} scores are then calculated across 8 values of $\rho = L^2 \cdot 2^{-i}$: $i \in \{-6, \dots, 1\}$. Figure 5 illustrates the returned $S_{\varepsilon}^{TV/KL}$. For reach $\sim L$ ($\rho \sim L^2$) the expected quadratic cost is maintained, where S_{ε}^{TV} meets the expected pure transport cost and S_{ε}^{KL} remains just below. It is expected for sufficiently high ρ S_{ε}^{KL} will achieve the expected cost. However, as ρ decreases to allow more relaxation in the marginals, the trend deviates. At some value of ρ it becomes cheaper to pay to destroy mass and change the marginals than pay the transport cost. In fact, in this simple setting, one can predict at what value of ρ the cost will change. Consider the 80 point separation case (C1C3). The pure transport cost would be $\frac{1}{2}(80)^2 \cdot 1345/1873.5 \sim 2300$ and the value at which the S_{ε}^{TV} cost changes from this is between $\rho = 2^{-3}L^2$ and $\rho = 2^{-4}L^2$. When the reach changes from 100 points to ~ 70 , i.e. when some points of C3 are deemed too far, this causes the marginal of the plan to change from the input (see Figure 4a and Figure 4b). These figures demonstrate that S_{ε}^{TV} is more robust in the reach parameter. This strict relationship is not found in the S_{ε}^{KL} cost where the penalisation is smoother. This matches the expected characteristics of TV and KL. Moreover, this explains S_{ε}^{KL} 's consistent underscoring of the expected $\frac{1}{2}W_2^2$ score, because it leads to a continuous marginal mass penalty. In summary, in the balanced scenario, the debiased cost is able to diagnose pure transport error, provided that

²All shifts are described from the centre of mass, and east from C1. These new cases supplement C1C1, C2C5/C3C5, C1C2/C2C3, C1C5, C1C3 which are at 20 increments.

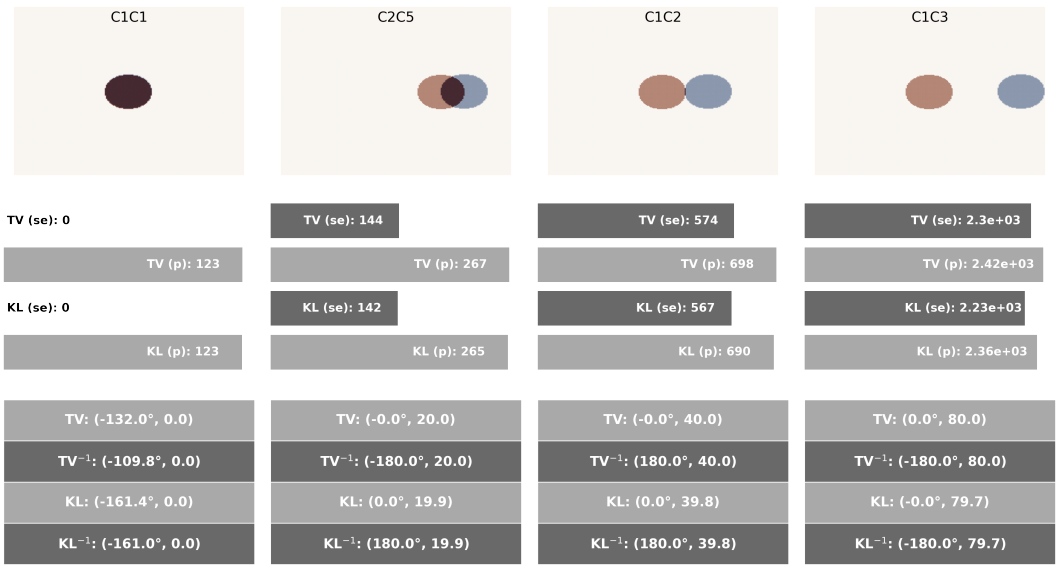
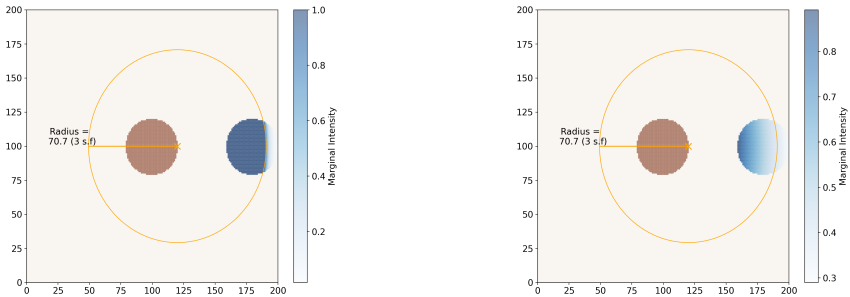


FIGURE 3 Cases which illustrate the similarity to $\frac{1}{2}W_2^2$ and show the quadratic translation relationship in the cost function (doubling the shift quadruples the cost). The top four horizontal bars display; $S_\epsilon^{TV}, UOT_\epsilon^{TV}, S_\epsilon^{KL}, UOT_\epsilon^{KL}$. The lower table presents the mean (ATD, ATM) in both flavours, and with the forward and inverse vectors. The red (darker) colour indicates observations, while the blue (lighter) represents forecasts. $\epsilon = 0.005 \cdot L^2, \rho = 1 \cdot L^2$.

the transported features are within the reach radius. For features outside this radius, it may be cheaper to destroy the mass instead, reducing the score. Through visualisation of the returned marginals it is possible to see which regions are being associated and which are too far.



(a) Illustration of TV penalty dependence on ρ for case C1C3. This shows where mass has been destroyed in the forecast marginal (blue), because mass that is too far is destroyed. For TV there is a strict link to the reach parameter. Note there is a 14.4% reduction in total intensity.

(b) Illustration of KL penalty dependence on ρ for case C1C3. The dependence on the reach is present, though in a more smooth fashion than for TV. Note there is a 45.9% reduction in total intensity.

FIGURE 4 Subfigures (a) and (b) contain the central observation C1 in red (lighter). The forecast is shifted 80 points to the right (C3) and the returned marginal, π_1 , is shown in blue (darker shades). The radius is the reach for $\rho = 2^{-4} \cdot L^2$, over which it is cheaper to destroy mass. The figures were generated for $\rho = 2^{-4} \cdot L^2, \epsilon = 0.005 \cdot L^2$.

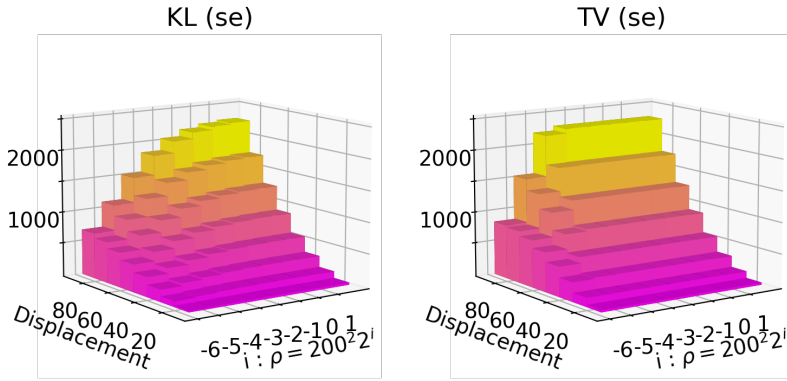


FIGURE 5 Reach sensitive study for case C1 vs C1 displaced east. Notice that a quadratic relation is maintained in the displacement for sufficiently large ρ . However, this changes as ρ decrease, and it becomes cheaper to destroy mass. S_ε^{TV} is more robust with a sharp drop-off in the reach dependence. x : ρ log scale, y : shift in grid points, z : Sinkhorn divergence. Left: S_ε^{KL} , Right: S_ε^{TV} . $\varepsilon = 0.005 \cdot L^2$.

4.1.4 | Multiple balanced features

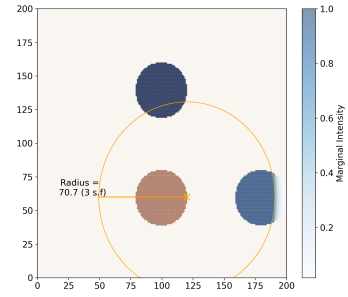
Figure 6a now considers cases C6C7 and C6C8 which each contain one "hit" and one "miss", and are still in the balanced setting. $S_\varepsilon^{KL/TV}$ reports similar values to C1C2 and C1C3, since it is scoring the complete match as close to zero. The $UOT_\varepsilon^{KL/TV}$ cost fails to diagnosis this hit due to bias. Observe that the ATM is half the shift of the miss, due to the fact that only half the points require transporting. The ATD remains close to 0 and 90 degrees. Crucially, the full hit pays no transport or mass destruction fee (see Figure 6b), whilst the miss is penalised depending on ρ and analogously to C1C3, i.e. there is an equivalent ρ radius of influence dependence for the southern event. It is important to note, that the hit's lack of cost is related to the zero transport required for the northern features, as opposed to the overlap. For example, C2C5 contains overlap, yet these points are shifted when the transport vectors are visualised. This is an important mathematical and behavioural distinction, from PAD, say, which a priori removes overlapped mass. This behaviour arises due to the strict convexity of entropic regularisation of the plan, which makes longer transport distances more expensive.

A further examination of the behaviour with multiple features is observed by the comparison between C6C12 and C1C2 (Figure S1a, and Figure 3). Note these are comparable since the total north-south shift of C6C12 cancels and their west-east shift is equally 40 grid points. Despite them having equivalent costs, they are discernable through the ATM and $UOT_\varepsilon^{KL/TV}$. C6C12 has each feature $20\sqrt{2} \sim 28.3$ apart, though with equal and opposite magnitude. This is reflected through zero average magnitude and arbitrary directions, which highlights a downfall of the ATM and ATD. Instead, considering the full distribution may offer more insight; this approach is taken in Skok and Lledó (2024).

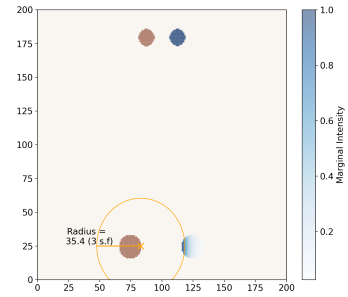
Additionally, through C13C14 (Figure S1a) it is possible to show that given sufficiently small reach parameter, one can dissociate features which are too far apart. Of course this is not directly reflected in the costs, however this is confirmed with visualisation of the approximate map (Figure S2). Moreover, by reducing the reach, a marginal with only the top feature retained is possible. The two southern events which are too far separated are regarded as too expensive to transport and instead their associated mass is destroyed (Figure 6c). This demonstrates a dissociation of features which are too far apart, defined through the choice of ρ .



(a) Demonstration that the logic of transportation holds when there is a hit and a miss present. The top four horizontal bars display S_{ϵ}^{TV} , UOT_{ϵ}^{TV} , S_{ϵ}^{KL} , UOT_{ϵ}^{KL} , respectively. The lower table presents the mean (ATD, ATM) in both flavours, and with the forward and inverse vectors. The red (darker) colour indicates observations, while the blue (lighter) represents forecasts. $\rho = 1 \cdot L^2$.



(b) Case C6C8 with TV marginal penalty. The marginal π_1 confirms there is a strict relationship with the reach parameter and it is maintained per feature. $\rho = 2^{-4} \cdot L^2$, the radius is equal to the reach.



(c) Case C13C14 with TV marginal penalty. The marginal π_1 shows that a distance feature can be removed if deemed too far separated, and this is maintained per feature. Here, the radius is equal to the reach, $\rho = 2^{-6} \cdot L^2$.

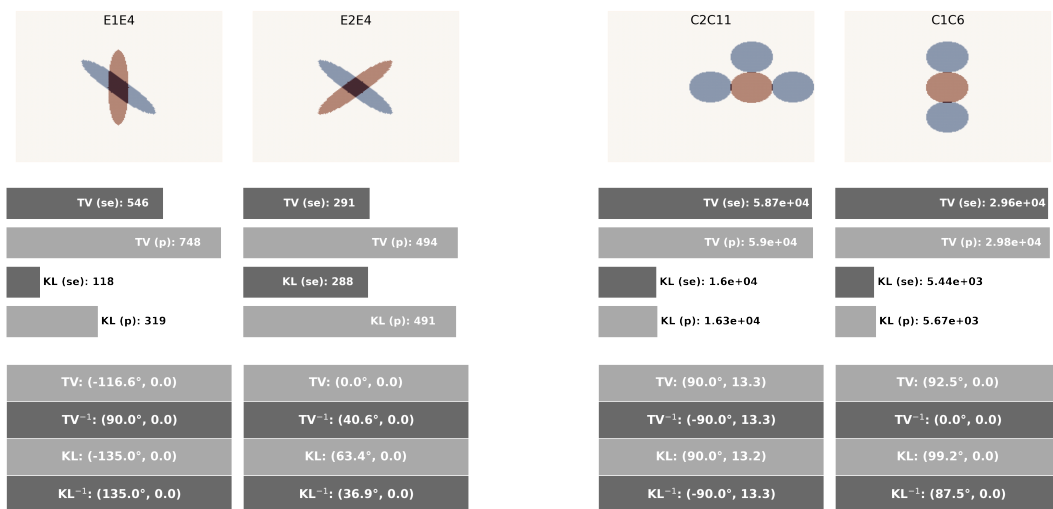
FIGURE 6 Figures exploring UOT's behaviour with multiple features present. (a) shows the scoring for cases with one hit and one miss which then moves away, and (b) and (c) show the returned marginals, π_1 , in blue (darker shades) with the observation in red (lighter). $\epsilon = 0.005 \cdot L^2$.

4.1.5 | Rotation and scale for balanced cases

Turning to consider rotation, it is known that UOT with the L2 cost function is not built to rotate objects which are at some angle to each other. By construction, the transport plan will stretch and squeeze the shapes to match (Figure S9 and Figure S8), mimicking the behaviour of quasi-rotation (or Aspect ratio) error, similar to geom004 (Ahijevych et al., 2009). To examine this, E1E4 vs E2E4 is compared against the pure transport case of E1E9, Figure 7a and Figure 2 respectively. E1E4 is scored significantly worse than E1E9 via S_{ϵ}^{TV} and better via S_{ϵ}^{KL} . For S_{ϵ}^{TV} most of the error appears in the marginal error terms, due to the imbalanced mass between E1 and E4. In contrast, S_{ϵ}^{KL} keeps this penalty term lower. For the 90° rotation, both flavours score worse than the pure transport, though now the mass is balanced so S_{ϵ}^{TV} scores this case better than E1E4, despite the rotation being larger. Notably, unlike CDST, $S_{\epsilon}^{TV/KL}$ is able to discern the two different rotations. CDST sees both rotations having the same centre of mass, causing a zero distance (this is also demonstrated in cases; C6C12, C1C6, C1C9 in Figures S1a, 7b and S3b). However, the ATM cannot distinguish E1E4 vs E2E4, because the transport is equal and opposite. On the other hand, S_{ϵ}^{KL} follows a similar trend to BDEL, where the scores indicate that E1E4 < E1E9 < E2E4. This does not imply that UOT can take into account rotation: it cannot. Although, S_{ϵ}^{KL} does appear to penalise the rotation in a way which may follow a more subjective evaluation. These cases further illustrate that S_{ϵ}^{TV} is sensitive to mass imbalance. This shall be seen to be

a major difference between the two flavours.

To complete the balanced cases, consider E6E14 and E2E10 (Figure S1b). Once more, the correct ATM and ATD are returned, with E6E14: $\sqrt{8^2 + 10^2} = 12.8$, and E2E10 : $\sqrt{15^2 + 20^2} = 25$. $S_\epsilon^{TV/KL}$ ranks them in the expected order: E6E14 scores better (lower) than E2E10 since less effort is required to correct the transport error, and the areal extent is smaller. Moreover, the scores directly scale with spatial extent and transport error, since E2 and E10 are 4 times larger than E6 and E14, and there is approximately twice the transport error (in squared Euclidean cost), hence $16.8 \cdot 4 \cdot 2^2 \sim 269$. This establishes that in the balanced setting, the methodology follows a predictable scaling between pairs of events.



(a) Rotated cases, E1E4 strictly is not balanced, though they are close in mass. UOT is not formulated to rotate shapes, instead stretches and squeezes them.

(b) Over-/under-forecasting area extent cases, providing an unbalanced setup. In comparison to C1C2 both of these cases are penalised much more.

FIGURE 7 Figures exploring rotation and over-/under- forecasting of events providing an imbalance of total intensities. The top four horizontal bars display: S_ϵ^{TV} , UOT_ϵ^{TV} , S_ϵ^{KL} , UOT_ϵ^{KL} . The lower table presents the mean (ATD, ATM) in both flavours, and with the forward and inverse vectors. The red (darker) colour indicates observations, while the blue (lighter) represents forecasts. $\epsilon = 0.005 \cdot L^2$, $\rho = 1 \cdot L^2$.

4.1.6 | Unbalanced scenarios

Changing focus to the unbalanced setting, Figure 7b exposes how the UOT methodology performs in systems where the rain coverage in the observation and forecast is different. Cases C1C6 and C2C11 relate to C1C2, since they can be viewed to be over- and under- forecasting, yet crucially without overlap. The Hausdorff distance and MED did not penalise this, as the fields maintain a maximal possible distance, and all three cases were scored equally. In contrast, UOT can differentiate these in the order C2C11 (worse), C1C6, C2C1 (best) with S_ϵ^{TV} returning more severe penalties. C1C6 then displays the expected ATM with equal and opposite transport, whilst C2C11 shows the west-east transport cancels, and the north-south remains, where noticeably 13.3 is one third of 40 (the transport in C1C2). Discernibly, more balanced spatial extents are favoured. This means that a forecaster is discouraged from hedging a forecast; this is harsher for the TV flavour. However, the weaker (yet still evident) penalisation by S_ϵ^{KL} may be more favourable to most users.

To analyse reach's effect in the unbalanced setting, consider the cases C1C6, C1C7, C1C8 (Fig. 7b and S3a), and their dependence to ρ in Figure 8c. In all these cases, S_e^{TV} is an order of magnitude larger than S_e^{KL} , and there is a small increase in the cost as the southern event becomes more displaced, i.e. the transport is being penalised. However, the cost is dominated by marginal error, or local adjustment of mass. In comparison to Figure 5, the dependence appears rotated in ρ and displacement, i.e. larger ρ enforces more balanced mass which is expensive in the unbalanced setting. Fortunately, the ATM picks up on the increased transport required, where due to the averaging the north-south transport has cancelled out and only the west-east transport remains. In fact, closer examination shows that the KL flavour favours the closer event, which appears as a skewed ATD (Figure S3a).

To investigate the reach further, consider Figure 8a and 8b. The returned marginals show that for the symmetric case of C1C6, the reach has an interpretation where half the mass is assigned evenly; the radius shown in Figure 8a is half the reach. Once this symmetry is broken, the top feature is attributed most of the available mass as it is closer, while the more distant feature is given a smaller portion, and only in the region closest to the observation. In this way, in the unbalanced setting, the linear interpretation of reach is not preserved. However, its understanding of assigning mass to closer features first is not lost. Altogether, this raises the question again of disintegration of the cost into its constituent terms to better diagnose different errors.

Through the comparison of cases (E3E11, E7E3, E7E11) in Figure 9, a fundamental insight can be gained. First, note that their value is subjective depending on the user. Second, these cases present common scenarios with a model over- or under- forecasting areal extent, given thresholding and whether the importance of overlap as well as extent is tested. UOT scores them across flavours in the ascending order: E3E11, E7E3, E7E11. E7E11 scores worse, though for the TV flavours it is below the shown significant figures. E3E11 returns close to the expected $\frac{1}{2} W_2^2$ cost, whereas the penalty paid for over-/under forecasting, a form of mass imbalance, dominates the other two cases. More compelling, though, is the small difference in scores between E7E3, E7E11. This provides utility as it means forecasters are not encouraged to increase overlap to hedge scores; it is more beneficial to match shapes and extent (and consequentially mass for these binary cases). Rather, balancing mass, thus reducing spatial bias, is a preferred strategy for minimising the UOT scores. This is in opposition to the distance metrics considered in Gilleland et al. (2020) which could all be hedged; most through increasing overlap.

This all comes with the caveats that results are reach dependent, and value is a subjective assessment, since some users may prefer E3E11 or E7E11. If this were the case, and absolute transport were more important to a user than intensity, spatial bias, and transport error combined, then this user could use the ATM solely. In this case, E7E3 is favoured since less transport is required, with a further disclaimer that in this case, the average has cancelled with equal and opposite transport vectors³.

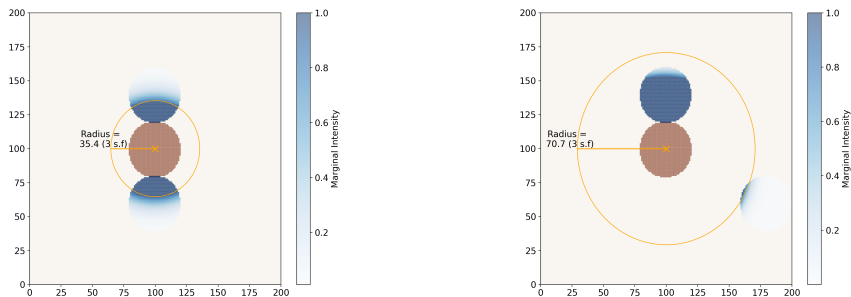
Finally, through the cases C1C9 and E19E20, it is clear that UOT cannot provide this information from the costs alone (Figure S3b). This is in contrast to MED which is able to diagnose if an event was a subset of another, by symmetry. An alternative interesting visualisation of a subset is the distribution of the transport vector's direction, since these will be spread across a full 360° if an event is a subset (Figure S5). It is important to notice that it is possible to create cases with a similar distribution which are not subsets. Hence, UOT's score is not able to discern subsets.

Until now only simple circles and ellipses have been considered, however a large benefit of the idealised cases is the opportunity to showcase a methodology's capacity (or deficiency) to cope with non-trivial fields, which we move towards next.

4.1.7 | Noisy, scattered and hole cases

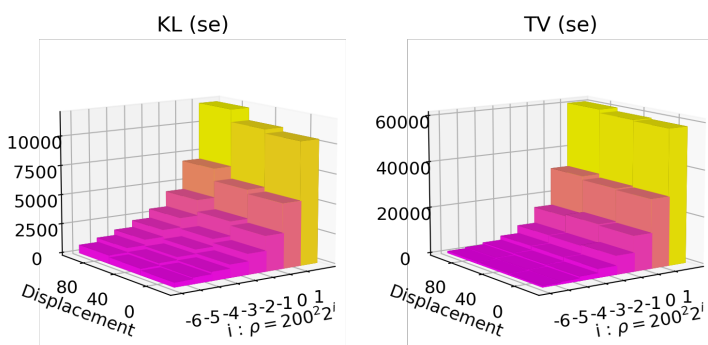
Cases S1S2, S1S3 in Figure 10 expose how a methodology copes with random scattered events contained within an envelope, imitating the occurrence of a collection of small showers. Since they are each distinct random realisations,

³Some readers may be interested to know that if E3 is given the same total intensity as E7, so that it becomes a balanced case again. Then E7E3 obtains a lower score due to less transport than E3E11.



(a) Case C1C6 with TV marginal penalty. The marginal π_1 shows again there is a strict relationship to the reach parameter although the mass is shared within half the reach. Hence the radius shown is equal to the reach.

(b) Case C1C8 with TV marginal penalty. The marginal π_1 shows the closer event is assigned more intensity whilst the distance feature in this unbalanced setting is given very little. The radius is equal to the reach.



(c) Reach sensitive study for case C1C6, C1C7, C1C8 which corresponds to a lower (southern) event being displaced away. This is now an unbalanced scenario and there is more extreme sensitivity to ρ than in the balanced setting. Notice that KL and TV have different scales. x: ρ log scale, y: shift in grid points, z: Sinkhorn divergence. Left: S_{ε}^{KL} , Right: S_{ε}^{TV} . $\varepsilon = 0.005 \cdot L^2$.

FIGURE 8 Overview of the marginals and debiased Sinkhorn divergence costing with ρ dependence for balanced displaced cases. Subfigures (a) and (b) contain central observation C1 in red (lighter). The forecast is shown in blue (darker shades). The radius is the reach for $\rho = 2^{-4} \cdot L^2$, over-which it is cheaper to destroy mass. The figures were generated for $\rho = 2^{-4} \cdot L^2$, $\varepsilon = 0.005 \cdot L^2$. Subfigure (c) provides a comparison of debiased Sinkhorn divergence costing.

the events do not have balanced mass and their relative mass is small compared to the scale M : S1 contains 185 non-zero points, S2 190 and S3 196. For S1S2, S_{ε}^{KL} behaves well, returning a low score as the features are contained within the same envelope, yet there is some associated cost of transport occurring. The ATM indicates 1.3 on average (2.1 Median average), aligning with MED and the fraction skill score, although these were able to diagnose closer to the average nearest neighbour transport distance between the two realisations, which is 2.35 (Gilleland et al., 2020). Conversely, S_{ε}^{TV} penalises these events fairly harshly, which from the above analysis is known to be due to mass imbalance. This trend continues in S1S3. For both flavours in these cases, ATM and ATD perform well. On the whole, these cases illustrate S_{ε}^{KL} is the more robust flavour of imbalance, and with greater capacity to cope with random scatter events.

Comparisons of C1N3, C1N4, N1N2 versus C1C4 (Figure11) reflect the situation that observations may not be clean, hence residual noise, or spurious points may remain even after cleaning. Without noise, C1C4 returns the

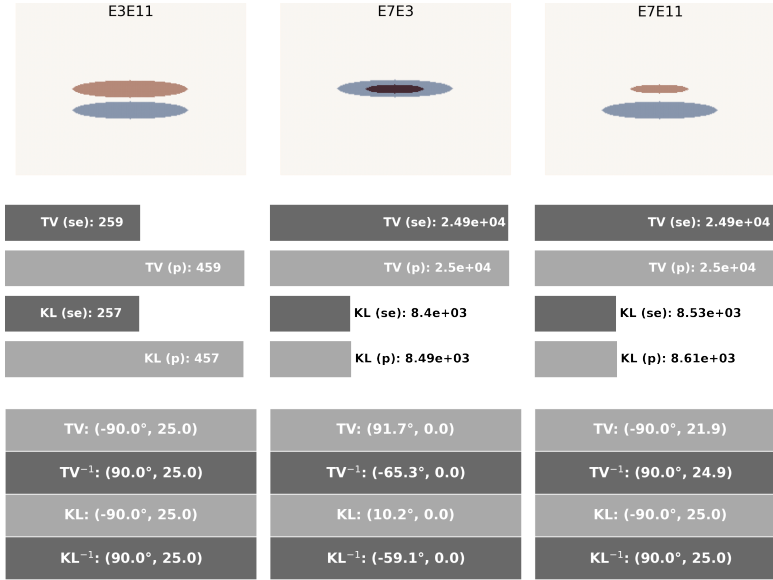


FIGURE 9 Comparison of subjective cases, exploring both balanced and unbalanced settings. Note that between E7E3 and E7E11 the TV scores¹ do increase, but below the shown significant figures. The top four horizontal bars display: S_{ε}^{TV} , UOT_{ε}^{TV} , S_{ε}^{KL} , UOT_{ε}^{KL} . The lower table presents the mean (ATD, ATM) in both flavours, and with the forward and inverse vectors. The red (darker) colour indicates observations, while the blue (lighter) represents forecasts. $\varepsilon = 0.005 \cdot L^2$, $\rho = 1 \cdot L^2$.

expected cost. After introducing noise, both flavours remain close to the known cost, ATM, and ATD, with S_{ε}^{KL} being more robust as expected. Yet both are still capable of diagnosing transport in the presence of a small amount of noise.

The Hole case H1H2, compared against C1C2, determines how a method performs with increased spatial matching and compliments to an event. Gilleland et al. (2020) made the observation that all the metrics they studied (bar Zhu's) preferred H1H2. UOT seems to offer similar behaviour, and $S_{\varepsilon}^{KL/TV}$ scores lower for H1H2 but not for $UOT_{\varepsilon}^{KL/TV}$. However, we believe the reasoning to be different since most of the points do not require any transport. Whilst it looks as though the same transport is occurring, the compliment to C1C2 has the option to move the dips between the two sets. In this way, the average transport occurring is the same, but the total squared Euclidean costing is not the same⁴. Considering the ATM, the returned score of 1.4 is correctly proportionally scaled against all those that do not move: $1.4 \sim 40 \cdot \frac{1345}{200^2 - 1345}$.

4.1.8 | Edge and extreme cases

Before moving onto real intensity forecasts, some attention is required for edge or extreme cases, such as very little to no precipitation or full precipitation over the whole domain. Purely from the optimisation interpretation, the null case has only one feasible plan that has a null marginal – the zero plan. In this scenario, all mass is destroyed in the non-zero field, hence the S_{ε}^{TV} and UOT_{ε}^{TV} can be defined though not the KL versions in a meaningful way, since zero scores are obtained. In neither flavour do the ATD and ATM make sense with null fields.

⁴Another way to see this is to take any 1D slice in the x-direction that goes across the dip. Since the dip is present, it will move along to fill the new set and the points behind it move, recreating the dip. However, the dip is closer to start with and so requires less transport. For example, consider the 1D sets [O, X, O, O, O, O] transporting to [O, O, O, O, X, O]. This requires X to move 3 points which is 9 units in squared Euclidean costings. Whilst [X, O, X, X, X, X] transporting to [X, X, X, X, O, X] requires 3 single points to move but only 1 costing each.

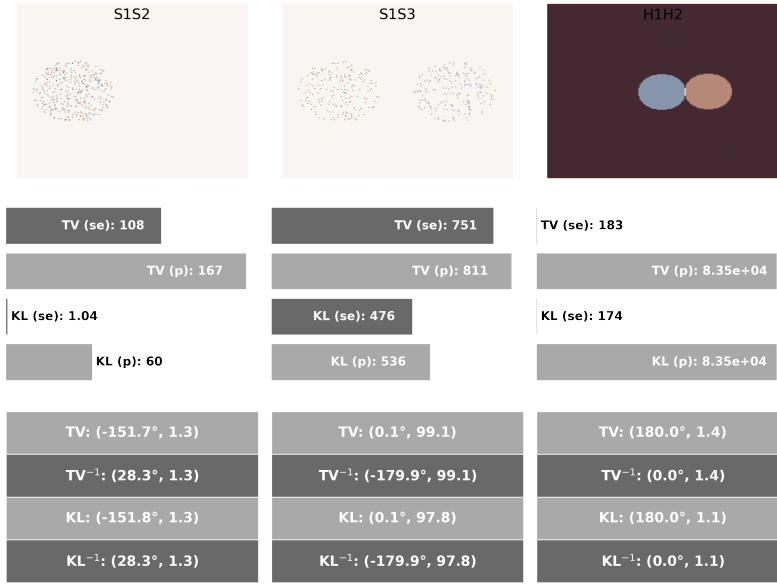


FIGURE 10 Scattered and compliment cases illustrating behaviour with small shower type events contained within an envelope and compliment logic or complete coverage with holes. The top four horizontal bars display; S_{ε}^{TV} , UOT_{ε}^{TV} , S_{ε}^{KL} , UOT_{ε}^{KL} . The lower table presents the mean (ATD, ATM) in both flavours, and with the forward and inverse vectors. The red (darker) colour indicates observations, while the blue (lighter) represents forecasts. $\varepsilon = 0.005 \cdot L^2$, $\rho = 1 \cdot L^2$.

For the completely covered fields, P2P2, the expected debiased cost of zero is returned (Figure S21). Then when comparing this full field with single point fields (P5, P3, P4 in Table 2) the costs are large due to a lot of mass modification and small average transport. These trends follow for P2P6. There are four points in P6, hence there is more mass available to distribute. The $S_{\varepsilon}^{TV/KL}$ is lower in this case, but not significantly.

For P3P4 the transport cost is expected as $199\sqrt{2} \sim 281.4$ which is seen in the ATM. In the balanced setting again S_{ε}^{TV} can attain the expected cost, whilst S_{ε}^{KL} is just below. When the reach is increased, both can achieve the expected score, whilst if it is reduced both eventually destroy mass. Notably, $UOT_{\varepsilon}^{KL/TV}$ and $S_{\varepsilon}^{KL/TV}$ are equal, since there is only one possible transport route between the two points.

In summary, the edge cases demonstrate that much of the previous logic holds, where pure transport is diagnosed, and UOT remains sensitive for single points to the expected transport. However, this behaviour is averaged with a larger number of points. Further, there are null cases which will need defining.

To conclude the binary geometric shapes, UOT has shown insensitivity to the relative boundaries position. It can also diagnose pure transport depending on the reach parameter, and hence it is robust to the double penalty problem. It is crucial that the debiased Sinkhorn divergence and transport plans are used, though disintegration of the cost may offer deeper diagnostics. Markedly, UOT prevents hedging and does not prioritise overlapping events. Instead, matching spatial extent is scored better by the metric. UOT is not able to pick up on purely rotational errors and fails to provide useful information under certain extreme cases, such as the null cases. Moreover, the cost itself is not diagnostic of subsets. In general, S_{ε}^{KL} appears to offer a more robust penalisation in the unbalanced setting. However, if (like Skok (2023)) both fields are normalised to the same mass, then S_{ε}^{TV} offers attractive features, especially when considering the link to the reach and the returned marginals of the plan. After this thorough exploration in a binary setting, let us turn to the real intensity cases.

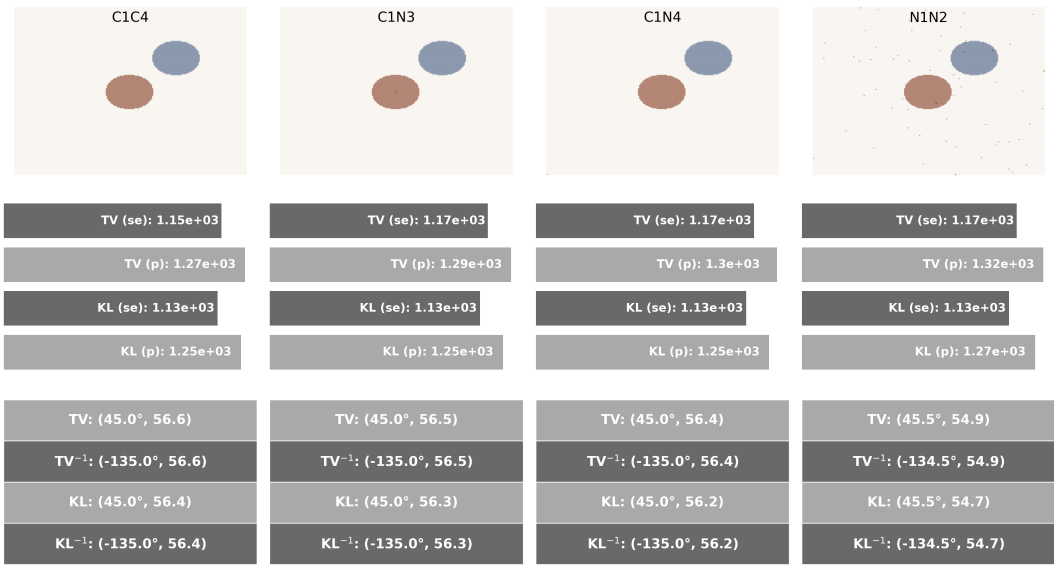


FIGURE 11 Noisy cases illustrating resistance to error in quality control or anomalous data depending on the type of marginal penalties. The top four horizontal bars display; $S_{\epsilon}^{TV}, UOT_{\epsilon}^{TV}, S_{\epsilon}^{KL}, UOT_{\epsilon}^{KL}$. The lower table presents the mean (ATD, ATM) in both flavours, and with the forward and inverse vectors. The red (darker) colour indicates observations, while the blue (lighter) represents forecasts. $\epsilon = 0.005 \cdot L^2, \rho = 1 \cdot L^2$.

Cases	Flavour	(se)	(p)	ATM	ATD	ATM (inv)	ATD (inv)
P2C1	tv	8.26E+05	8.28E+05	5.97E-01	-135.0	1.47E-08	45.0
P2C1	kl	5.79E+05	5.81E+05	6.97E-01	-135.0	6.43E-01	45.0
P2P5	tv	8.55E+05	8.54E+05	7.07E-01	-135.0	5.55E-11	45.0
P2P5	kl	8.99E+05	8.46E+05	7.07E-01	-135.0	6.53E-01	45.0
P2P6	tv	8.55E+05	8.54E+05	1.45E-14	-141.3	3.39E-14	125.0
P2P6	kl	8.91E+05	8.38E+05	2.29E-15	-83.5	7.68E-14	-139.4
P3P4	tv	2.11E+01	2.18E+01	2.81E+02	45.0	2.81E+02	-135.0
P3P4	kl	1.64E+01	1.71E+01	2.81E+02	45.0	2.81E+02	-135.0
P6P7	tv	1.03E+01	1.31E+01	3.54E-01	-135.0	3.54E-01	45.0
P6P7	kl	9.79E+00	1.25E+01	1.82E-01	-135.0	9.53E-02	45.0

TABLE 2 Table of costings for the extreme and edge cases given $\epsilon = 0.005 \cdot L^2, \rho = 1 \cdot L^2$. See Table 1 for the description of the cases used here.

4.2 | Real Intensity Cases

Given the observations above, the natural proceeding question is if these behaviours and properties extend into real intensity textures and shapes. To begin to answer this, let us study the comparisons between fake000 and fake001-fake005, where since the observation is the same for all comparisons, M is chosen as the total mass of fake000

(356100.0), L is set as 601 to keep the cost function $O(1)$ and $\varepsilon = 0.001 \cdot L^2$ chosen appropriately given the mesh. As in the binary cases, the $S_\varepsilon^{KL/TV}$ score is expected to quadruple between each case – irrespective of the intensity now being taken into consideration – and the ATM and ATD should follow the known displacement (with the caveat that these cases are not perfectly balanced).

4.2.1 | Fake cases

Figure 12 (with $\rho = L^2$) shows there is again a pronounced difference between the two flavours. For reference, the expected S_ε score for fake000fake001 is approximately $16.9 \sim 0.5 \cdot (3^2 + 5^2) \cdot 354859/356100$ (as these cases are no longer balanced and so the exact cost is not known). Hence, S_ε^{KL} is appearing more robust, staying close to the expected score and approximately following the quadratic relation between the cases. On the other hand, S_ε^{TV} is overly penalising the forecasts and there is no quadratic relationship because the marginal penalty terms dominate the costing. Interestingly, this sensitivity is reduced when the reach is reduced so that transport is kept local (Figure S10 where reach is $2^{-6} \cdot L$). Now S_ε^{TV} improves its cost, though the expected quadratic relation is still not recovered. Examining the ATM and ATD, the expected ATM is 5.8, approximately doubling sequentially, (11.7, 23.3, 46.6, 93.3), and in the forward direction at a maintained -59° . For both flavours the ATM and ATD are close, however looking at the median averages (Figure S11 and Figure S12) this becomes more evident. For smaller reach and smaller displacement the diagnostic is closer to the known perturbation, though at the larger perturbations this diagnostic fails since the reach has been reduced. This reconfirmed $S_\varepsilon^{KL/TV}$'s expected behaviour, yet with nonuniform intensities.

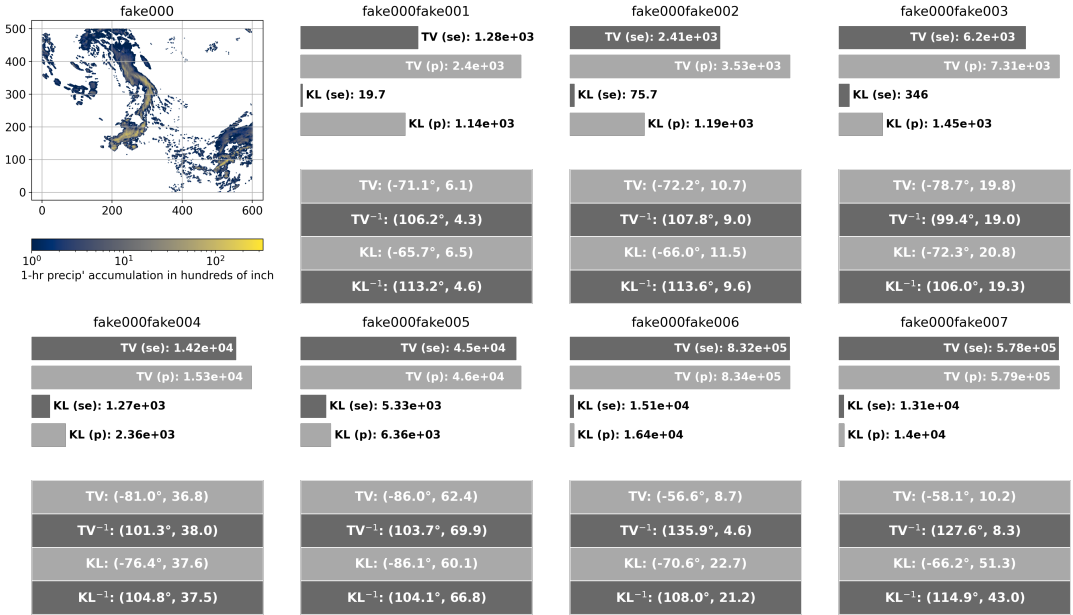


FIGURE 12 Perturbed cases with real textured intensities. All cases are a changed version of fake000, shown in the top left. The top four horizontal bars display: S_ε^{TV} , UOT_ε^{TV} , S_ε^{KL} , UOT_ε^{KL} . The lower table presents the mean (ATD, ATM) in both flavours, and with the forward and inverse vectors. The red (darker) colour indicates observations, while the blue (lighter) represents forecasts. $\varepsilon = 0.001 \cdot L^2$, $\rho = L^2$, reach ~ 849 .

A further visualisation tool, following (Marzban et al., 2009) and optical flow techniques, is a 2D histogram of the underlying transport vectors' direction and magnitude. This is a more powerful diagnostic tool than simple summary metrics like ATM and ATD which have been shown to oversimplify some cases. Figure 13, illustrates that debiasing

corrects the vectors and concentrates them towards the true ATM, ATD; this is true of both S_ϵ^{KL} and S_ϵ^{TV} . Two observations are key. First, the debiased case is able to successfully diagnose the correct angle and magnitude from the approximate mapping yet now with the inclusion of real intensities. Second, that debiasing is crucial to be able to draw conclusions. Both have been highlighted throughout the above investigation.

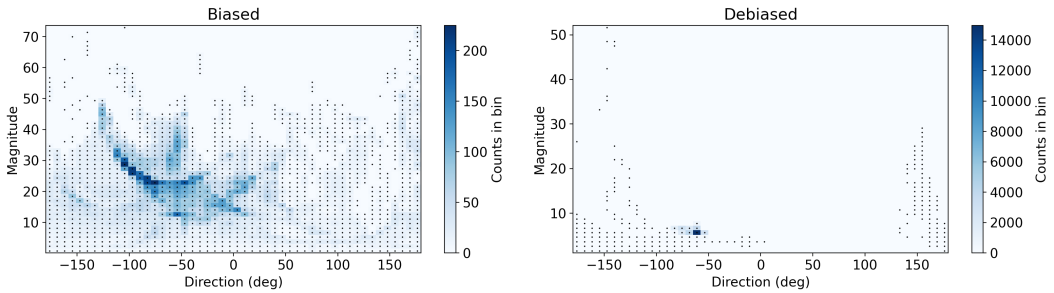


FIGURE 13 2D histogram of the magnitude and direction of the underlying transports vectors for the perturbed case fake000fake001, which has expected transport cost at -59° and 5.8 points. The dotted bins, indicate those with non-zero mass. These results are based on TV with parameters $\epsilon = 0.001 \cdot L^2$, $\rho = L^2$.

The last of the real textured perturbed cases are fake006 and fake007. Now the ATD is well maintained at the expected angle, however the ATM is not well-preserved nor does it appear to scale with the change in mass ($\sim 44\%$, -32% respectively). Fortunately all the scores are penalised more than fake000fake003, and depending on the reach (and thus importance of transport) and flavour they score differently against fake004 and fake005. Whilst this may seem like complex behaviour, it allows selection of priorities by picking the appropriate formulation. That is, if imbalance is allowed and above a certain reach the forecast should be penalised more, by setting the parameter appropriately one can order these cases differently. Notably, fake006 always costs more than fake007 for TV penalisation which follows the size of mass imbalance. However, KL penalisation changes with the reach, and for smaller reach (allowing cheaper mass destruction) fake006 can cost less than fake007. From the scores alone, the direction of imbalance is not diagnosable, i.e. the mass of fake006 is greater than fake000 which is greater than fake007. However, when the cost function terms are broken down, then comparison of the terms $D(\pi_0|\mu_O)$ and $D(\pi_1|\mu_F)$ does indicate a direction (this exploration goes beyond the scope of the current paper). This highlights the potential for disintegration of the cost terms themselves. Crucially, with real intensities and textured data there is still the possibility to diagnose pure transport error and be robust against the double penalty problem.

4.2.2 | Spring 2005 cases

The final dataset considers real model evaluations of 3 models against observations. Here the in-sample average gives $M = 200464$. See Figure 14 for the costs results from our methodology. The experts' subjective evaluation ordered the models (wrf4ncar, wrf2caps, wrf4ncep) in increasing score or better to worse. Across flavours, S_ϵ followed in agreement with this ordering predominantly, and on mean (and median) average. In fact, 8 out of 9 of the time periods agreed on the top ranking model. There are two large anomalies: May 19, where wrf4ncar and wrf2caps perform worse than wrf4nceps, and May 25 where wrf4ncar performs worse than wrf2caps. Looking at the breakdown of the scores in Table 3 of Keil and Craig (2009) these same irregularities are found, though on May 25th the experts order them (wrf2caps, wrf4ncep, wrf4ncar). Significantly, these two anomalies also correspond with two notable differences in the balance of mass. On May 19th there is a significant over forecast from all the models, shown in Figure 4 of (Ahijevych et al., 2009). Then on May 25th wrf2caps and wrf4ncar under forecast, and notably both failed to pick up on a feature in the north-west, which wrf4ncep did forecast (see Figure S14). This is reflected in the large ATM

for wrf2caps and wrf4ncar (see Figure S13) since the failure to predict this feature means this mass is transported to the next closest feature, which is far away. On average, $S_{\varepsilon}^{KL/TV}$ follows subjective scoring and is able to pick up on anomalies which are diagnosable through further investigative techniques under the same methodology.

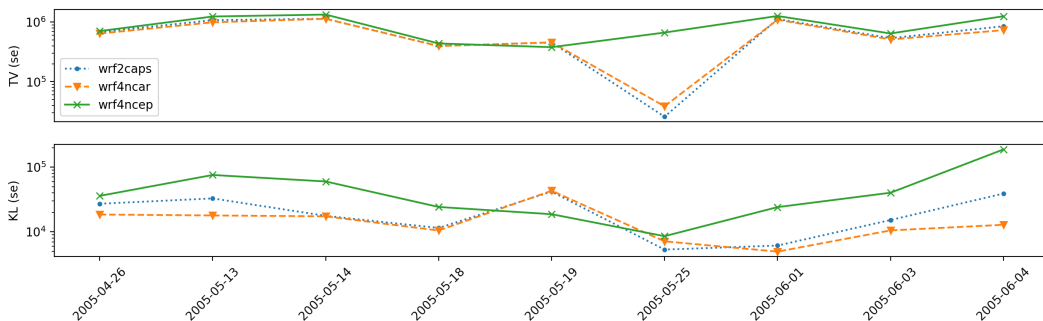


FIGURE 14 Spring 2005 cases scores for 9 time stamps. Notice the different in scale between S_{ε}^{TV} (top) and S_{ε}^{KL} (bottom), where mostly the models rankings are in agreement. However, there are clear anomalies at key dates: 2005-05-25 and 2005-05-19. Each model was at 24hr lead time, and interpolated on the coarser 4km grid. $\varepsilon = 0.001 \cdot L^2$, $\rho = L^2$.

5 | CONCLUSIONS AND FURTHER WORK

Throughout the above discussion, UOT has been shown to possess many desirable properties as a spatial precipitation forecast verification metric and associated toolbox. Imperatively, the debiased Sinkhorn divergence was shown to be robust to the double penalty problem and capable of diagnosing spatial errors in a forecast-observation pair. It was shown to diagnose known translational error in the correct units of length for both binary and real textured forecasts. In the balanced cases, where the total area and level is equal in the two fields, both types of marginal penalties (TV and KL) were shown to be competent at diagnosing frequency error, or shape bias, and translational error. One major benefit in this setting is S_{ε}^{TV} 's geometric link with the reach parameter. Here, a user may define a strict distance above which a feature becomes disassociated and instead that mass is modified. This reflects a skill-scale similar to Cluster Analysis, which uses the number of clusters to define skill (Marzban et al., 2009). Whilst S_{ε}^{KL} did not possess such a strict relationship to the reach parameter, it did show effectiveness in the presence of spatial biases and noise. That is, in the unbalanced scenarios S_{ε}^{KL} was shown to be more robust, both to small amounts of noise in the presence of translation error and to over-/under- forecasting. This property carried from the simple binary forecasts into the real textured data.

Unfortunately, UOT was demonstrated as not being able to diagnose rotational error. Rather, stretching and squeezing of a shape is undertaken, thus mimicking an aspect-ratio error correction. This is due to the convex nature of the optimal map. One potential solution is to separately optimise the rotation, like MODE (Davis et al., 2006), or even explicitly include rotation as part of the optimisation argument.

Further, UOT is not able to diagnose if a pair has one component being a subset of another. Such a scenario may be beneficial to differentiate, say, forecasts E3E11 versus E7E3, since depending on the user the value changes. This comes with the optimism that behind the UOT cost there are 11 terms themselves diagnostic of different behaviour, though their full exploration goes beyond this current work.

Some simpler geometric properties which were exemplified included insensitivity to zero points and, as a result, to the domain boundary. Orientation on the regular grid showed some sensitivity, but it was not significant nor detrimental, while also little sensitivity to orientation was shown, considering that all these cases lie on a regular grid.

Moreover, throughout the test cases, it was illustrated vehemently that UOT cannot be hedged. UOT is performing transport and will move overlap to optimally assign regions of rain. Hence, if necessary, it will move overlap to reduce the overall cost. By preference, then, UOT favours pairs which have balanced total mass and minimal transport. Although through the real textured cases, it was shown that by careful selection of the reach parameter, the importance associated to mass balance and translation can be changed.

Lastly, and most crucially, the Sinkhorn divergence in both flavours was shown to follow subjective evaluation of real model performance, on average. Furthermore, through identification of anomalies in the series, a more detailed exploration was enabled, calling attention to model runs which were both significantly imbalanced and missing a particular feature. A recommended practice for its use would then be to encourage a similar procedure. The Sinkhorn divergence can be calculated for a series or set of pairs, along with the ATM and ATD, as biproducts. Given any anomalies in this series, a more detailed exploration can be undertaken for specific time stamps. Further, in the research setting and given more computational expense (or less time constraints) a parameter sweep in the reach may be performed, with marginals returned spotlighting a scale of skill and at what reach certain features are no longer associated.

5.1 | Further Work

Finally, while this current work is meant as an initial investigation into the potential behind precipitation forecast verification with the Sinkhorn divergence and its various tools, there is still much to consider, all contained within the same or similar framework. Notably, and what was briefly mentioned, is that UOT is capable of having the observation-forecast pair on different grids. However, a thorough exploration of the effects and their influence on the costings would be needed for confidence to be given to the score. Alongside the so-far mentioned tools, there is also the possibility of looking into the disintegration of the terms and taking a similar infographic route as SAL and DAS, where terms corresponding to separate information are plotted to allow for diagnosis of different errors, such as transport vs. spatial bias and ranking. Moreover, through numerical efficiency tricks, it is possible to capture information at successfully finer scales.

A further development would be turning the negatively oriented cost into a skill score. This could be against some random realisation over the domain, or climatology, or by considering bounds on the cost and using them to recentre the values. Additionally, there are many marginal penalisation terms available beyond just KL and TV divergences. Or even the possibility to include topographical or location-based reach parameters, relating features which are geographically associated, but stopping (say over mountain ranges) features that should not be related.

Lastly, there is a strong capability for this methodology to extend into ensemble space. Underpinning all the mathematics is the extension to multi-marginal optimal transport (Benamou, 2021; Beier et al., 2022), where each marginal would correspond to a member and one for the observation. This would leverage conditional information on every member as well as granting access to a related problem of finding Wasserstein Barycentres, which are a transport-informed type of averaging, unlike the typical L^1 average.

6 | SUPPORTING INFORMATION

The supplementary material, S1, contains details of our implementation (Section S1.1) efficiency tricks used including Tensorisation and epsilon-annealing (Section S1.1.1), as well as supporting figures (Section S1.2), and missing cases to match those examined in Gilleland et al. (2020) (Section S1.3).

All figures are as follows; Cases C6C12 and C13C14, Fig. S1a, Cases E6E14 and E2E10 Fig. S1b, Transport vector illustration for case C13C14 Fig. S2. Illustration of cases C1C7, and C1C8, Fig. S3a, subset events C1C9 E19E20 Fig. S3b, C1C6 KL marginal, Fig. S4a, C1C6 TV marginal, Fig. 8a, C1C9 2D histogram Fig. S5, E19E20 2D histogram

Fig. S6, E20E19 2D histogram Fig. S7. Transport vector illustration for rotation in case E2E4 in TV, fig. S8, and KL fig. S9. Perturbed real cases: Fig. S10 with $\rho = 2^{-6}$, and Fig. S11 and Fig. S12 are demonstration of Fig. 12 and Fig. S10 with a median average ATM and ATD. Fig. S13 shows the ATM complimenting Fig. 14 and Fig. S14 presents the graphical abstract image. Subsequent figures fill in missing cases: C3C5, C1C10, C3C4. C3C5, C3C4, in Fig. S15, E4E8, E6E16, E2E17, E4E12, in Fig. S16, E4E10, E4E14, E1E3, E1E13, in Fig. S17, E5E7, E2E18, E2E6, E1E11, in Fig. S18, E2E16, E1E14, in Fig. S19, P1C1, P2P6, P1P5, P1P3 in Fig. S20, P2P2, P2P5, P1P2, P1P1, in Fig. S21, P2C1, P6P7, P1P4, in Fig. S22.

References

- Ahijevych, D., Gilleland, E., Brown, B.G., Ebert, E.E., 2009. Application of Spatial Verification Methods to Idealized and NWP-Gridded Precipitation Forecasts. *Weather and Forecasting* 24, 1485–1497. doi:10.1175/2009WAF2222298.1.
- Beier, F., von Lindheim, J., Neumayer, S., Steidl, G., 2022. Unbalanced Multi-marginal Optimal Transport. *Journal of Mathematical Imaging and Vision*, 1–20doi:10.1007/s10851-022-01126-7/FIGURES/5.
- Benamou, J.D., 2021. Optimal transportation, modelling and numerical simulation. doi:10.1017/S0962492921000040.
- Benamou, J.D., Brenier, Y., 1998. Weak Existence for the Semigeostrophic Equations Formulated as a Coupled Monge–Ampère/Transport Problem. *SIAM Journal on Applied Mathematics* 58, 1450–1461. doi:10.1137/S0036139995294111.
- Benamou, J.D., Brenier, Y., 2000. A computational fluid mechanics solution to the Monge-Kantorovich mass transfer problem. *Numerische Mathematik* 2000 84:3 84, 375–393. doi:10.1007/s002110050002.
- Benamou, J.D., Martinet, M., 2020. Capacity Constrained Entropic Optimal Transport, Sinkhorn Saturated Domain Out-Summation and Vanishing Temperature .
- Berman, R.J., 2020. The Sinkhorn algorithm, parabolic optimal transport and geometric Monge–Ampère equations. *Numerische Mathematik* 145, 771–836. doi:10.1007/s00211-020-01127-x.
- Bocquet, M., Vanderbeeken, P.J., Farchi, A., Dumont Le Brazidec, J., Roustan, Y., 2024. Bridging classical data assimilation and optimal transport: the 3D-Var case. *Nonlinear Processes in Geophysics* 31, 335–357. doi:10.5194/npg-31-335-2024.
- Brown, B.G., Gilleland, E., Ebert, E.E., 2011. Forecasts of Spatial Fields. *Forecast Verification*, 95–117doi:10.1002/9781119960003.CH6.
- Casati, B., Ross, G., Stephenson, D.B., 2004. A new intensity-scale approach for the verification of spatial precipitation forecasts. *Meteorol. Appl* 11, 141–154. doi:10.1017/S1350482704001239.
- Charlier, B., Feydy, J., Glaunès, J.A., . Kernel Operations on the GPU, with autodiff, without memory overflows – KeOps. URL: <https://www.kernel-operations.io/keops/index.html>.
- Charlier, B., Feydy, J., Glaunès, J.A., Collin, F.D., Durif, G., 2021. Kernel Operations on the GPU, with Autodiff, without Memory Overflows. *Journal of Machine Learning Research* 22, 1–6. URL: <http://jmlr.org/papers/v22/20-275.html>.
- Chizat, L., 2024. Annealed Sinkhorn for Optimal Transport: convergence, regularization path and debiasing URL: <http://arxiv.org/abs/2408.11620>.
- Chizat, L., Peyré, G., Schmitzer, B., Vialard, F.X., 2016. Scaling Algorithms for Unbalanced Transport Problems doi:10.48550/arxiv.1607.05816.
- Cuturi, M., 2013. Sinkhorn Distances: Lightspeed Computation of Optimal Transport, in: Burges, C.J., Bottou, L., Welling, M., Ghahramani, Z., Weinberger, K.Q. (Eds.), *Advances in Neural Information Processing Systems*, Curran Associates, Inc. URL: https://proceedings.neurips.cc/paper_files/paper/2013/file/af21d0c97db2e27e13572cbf59eb343d-Paper.pdf.
- Davis, C.A., Brown, B., Bullock, R., 2006. Object-Based Verification of Precipitation Forecasts. Part I: Methodology and Application to Mesoscale Rain Areas. *Monthly Weather Review* 134, 1772–1784. doi:10.1175/MWR3145.1.

- Davis, C.A., Brown, B.G., Bullock, R., Halley-Gotway, J., 2009. The Method for Object-Based Diagnostic Evaluation (MODE) Applied to Numerical Forecasts from the 2005 NSSL/SPC Spring Program. *Weather and Forecasting* 24, 1252–1267. doi:10.1175/2009WAF2222241.1.
- Dorninger, M., Gilleland, E., Casati, B., Mittermaier, M.P., Ebert, E.E., Brown, B.G., Wilson, L.J., 2018. The Setup of the MesoVICT Project. *Bulletin of the American Meteorological Society* 99, 1887–1906. doi:10.1175/BAMS-D-17-0164.1.
- Ebert, E.E., 2008. Fuzzy verification of high-resolution gridded forecasts: a review and proposed framework. *Meteorological Applications* 15, 51–64. doi:10.1002/met.25.
- Eric Gilleland, n.d. Spatial Forecast Verification Reference List. URL: <https://projects.ral.ucar.edu/icp/references.html>.
- Farchi, A., Bocquet, M., Roustan, Y., Mathieu, A., Qu  rel, A., 2016. Using the Wasserstein distance to compare fields of pollutants: application to the radionuclide atmospheric dispersion of the Fukushima-Daichi accident. *Tellus B: Chemical and Physical Meteorology* doi:10.3402/tellusb.v68.31682.
- Feydy, J., Roussillon, P., . Geometric Loss functions between sampled measures, images and volumes – GeomLoss. URL: <https://www.kernel-operations.io/geomloss/index.html>.
- Feydy, J., S  journ  , T., Vialard, F.X., Amari, S.i., Troune, A., Peyr  , G., 2019. Interpolating between Optimal Transport and MMD using Sinkhorn Divergences, in: Chaudhuri, K., Sugiyama, M. (Eds.), *Proceedings of the Twenty-Second International Conference on Artificial Intelligence and Statistics*, PMLR. pp. 2681–2690. URL: <https://proceedings.mlr.press/v89/feidy19a.html>.
- Feyeux, N., Vidard, A., Nodet, M., 2018. Optimal transport for variational data assimilation. *Nonlinear Processes in Geophysics* 25, 55–66. doi:10.5194/npg-25-55-2018.
- Flamary, R., Courty, N., Gramfort, A., Alaya, M.Z., Boisbunon, A., Chambon, S., Chapel, L., Corenflos, A., Fatras, K., Fournier, N., Gautheron, L., Gayraud, N.T.H., Janati, H., Rakotomamonjy, A., Redko, I., Rolet, A., Schutz, A., Seguy, V., Sutherland, D.J., Tavenard, R., Tong, A., Vayer, T., 2021. POT: Python Optimal Transport. *Journal of Machine Learning Research* 22, 1–8. URL: <http://jmlr.org/papers/v22/20-451.html>.
- Francis, J., n.d. UOTforSpatialVerification: Unbalanced Optimal transport implementation with total variation or Kullback-Leibler marginal penalisation for Precipitation forecast verification. URL: <https://github.com/Jacob-Francis/UOTforSpatialVerification>.
- Gilleland, E., 2011. SpatialVx: Spatial Forecast Verification. URL: <https://CRAN.R-project.org/package=SpatialVx>, doi:10.32614/CRAN.PACKAGE.SPATIALVX.
- Gilleland, E., Ahijevych, D., Brown, B.G., Casati, B., Ebert, E.E., 2009. Intercomparison of Spatial Forecast Verification Methods. *Weather and Forecasting* 24, 1416–1430. doi:10.1175/2009WAF2222269.1.
- Gilleland, E., Ahijevych, D.A., Brown, B.G., Ebert, E.E., 2010. Verifying forecasts spatially. *Bulletin of the American Meteorological Society* 91, 1365–1373. doi:10.1175/2010BAMS2819.1.
- Gilleland, E., Skok, G., Brown, B.G., Casati, B., Dorninger, M., Mittermaier, M.P., Roberts, N., Wilson, L.J., 2020. A Novel Set of Geometric Verification Test Fields with Application to Distance Measures. *Monthly Weather Review* 148, 1653–1673. doi:10.1175/MWR-D-19-0256.1.
- Gramfort, A., Peyr  , G., Cuturi, M., 2015. Fast Optimal Transport Averaging of Neuroimaging Data, in: Ourselin, S., Alexander, D., Westin, C., Cardoso, M. (Eds.), *Information Processing in Medical Imaging*, Springer International Publishing, Cham. pp. 261–272.
- Grauman, K., Darrell, T., 2005. The pyramid match kernel: discriminative classification with sets of image features, in: *Tenth IEEE International Conference on Computer Vision (ICCV'05) Volume 1*, pp. 1458–1465. doi:10.1109/ICCV.2005.239.
- Hou, A.Y., Kakar, R.K., Neeck, S., Azarbarzin, A.A., Kummerow, C.D., Kojima, M., Oki, R., Nakamura, K., Iguchi, T., 2014. The Global Precipitation Measurement Mission. *Bulletin of the American Meteorological Society* 95, 701–722. doi:10.1175/BAMS-D-13-00164.1.

- Hyun, S., Mishra, A., Follett, C.L., Jonsson, B., Kulk, G., Forget, G., Racault, M.F., Jackson, T., Dutkiewicz, S., Müller, C.L., Bien, J., 2022. Ocean movers distance: using optimal transport for analysing oceanographic data. *Proceedings of the Royal Society A* 478. doi:10.1098/RSPA.2021.0875.
- Kain, J.S., Weiss, S.J., Bright, D.R., Baldwin, M.E., Levit, J.J., Carbin, G.W., Schwartz, C.S., Weisman, M.L., Drogemeier, K.K., Weber, D.B., Thomas, K.W., 2008. Some Practical Considerations Regarding Horizontal Resolution in the First Generation of Operational Convection-Allowing NWP. *Weather and Forecasting* 23, 931–952. doi:10.1175/WAF2007106.1.
- Kantorovitch, L., 1958. On the Translocation of Masses. *Management Science* 5, 1–4. URL: <http://www.jstor.org/stable/2626967>.
- Keil, C., Craig, G.C., 2007. A Displacement-Based Error Measure Applied in a Regional Ensemble Forecasting System. *Monthly Weather Review* 135, 3248–3259. doi:10.1175/MWR3457.1.
- Keil, C., Craig, G.C., 2009. A Displacement and Amplitude Score Employing an Optical Flow Technique. *Weather and Forecasting* 24, 1297 – 1308. doi:10.1175/2009WAF2222247.1.
- Kolouri, S., Park, S.R., Thorpe, M., Slepcev, D., Rohde, G.K., 2017. Optimal Mass Transport: Signal processing and machine-learning applications. *IEEE Signal Processing Magazine* 34, 43–59. doi:10.1109/MSP.2017.2695801.
- Liero, M., Mielke, A., Savaré, G., 2016. Optimal transport in competition with reaction: The Hellinger-Kantorovich distance and geodesic curves. *SIAM Journal on Mathematical Analysis* 48, 2869–2911. doi:10.1137/15M1041420.
- Lin, Y., Mitchell, K.E., 2005. The NCEP Stage II/IV Hourly Precipitation Analyses: Development and Applications, in: *Proceedings of the 19th Conference on Hydrology*, American Meteorological Society, San Diego, CA, USA.
- Liu, X., Frank, J., 2022. Ensemble data assimilation using optimal control in the Wasserstein metric. *Journal of Computational Science* 65, 101895. doi:10.1016/J.JOCS.2022.101895.
- Lucas, B.D., Kanade, T., 1981. An Iterative Image Registration Technique with an Application to Stereo Vision, in: *IJCAI'81: 7th international joint conference on Artificial intelligence*, Vancouver, Canada, pp. 674–679. URL: <https://hal.science/hal-03697340>.
- Magyar, J.C., Sambridge, M., 2023. Hydrological objective functions and ensemble averaging with the Wasserstein distance. *Hydrology and Earth System Sciences* 27, 991–1010. doi:10.5194/hess-27-991-2023.
- Marzban, C., Sandgathe, S., 2010. Optical Flow for Verification. *Weather and Forecasting* 25, 1479–1494. doi:10.1175/2010WAF2222351.1.
- Marzban, C., Sandgathe, S., Lyons, H., Lederer, N., 2009. Three spatial verification techniques: Cluster analysis, variogram, and optical flow. *Weather and Forecasting* 24, 1457–1471. doi:10.1175/2009WAF2222261.1.
- Mass, C.F., Ovens, D., Westrick, K., Colle, B.A., 2002. DOES INCREASING HORIZONTAL RESOLUTION PRODUCE MORE SKILLFUL FORECASTS?: The Results of Two Years of Real-Time Numerical Weather Prediction over the Pacific Northwest. *Bulletin of the American Meteorological Society* 83, 407–430. doi:10.1175/1520-0477(2002)083<0407:DIHRPM>2.3.CO;2.
- Méridot, Q., Thibert, B., 2020. Optimal transport: discretization and algorithms. *Handbook of Numerical Analysis* 22, 133–212. doi:10.1016/bs.hna.2020.10.001.
- Mittermaier, M., Roberts, N., Thompson, S.A., 2013. A long-term assessment of precipitation forecast skill using the Fractions Skill Score. *Meteorological Applications* 20, 176–186. doi:10.1002/MET.296.
- Monge, G., 1781. Mémoire sur la théorie des déblais et des remblais. URL: <https://search.worldcat.org/title/Memoire-sur-la-theorie-des-deblais-et-des-remblais/oclc/51928110>.
- Murphy, A.H., 1993. What Is a Good Forecast? An Essay on the Nature of Goodness in Weather Forecasting. *Weather and Forecasting* 8, 281–293. doi:https://doi.org/10.1175/1520-0434(1993)008<0281:WIAGFA>2.0.CO;2.
- NCAR, n.d. RAL | JNT | Forecast Evaluation and Applied Statistics | Spatial Forecast Methods Inter-Comparison Project (ICP/MesoVICT). URL: <https://projects.ral.ucar.edu/icp/>.

- Nishizawa, S., 2024. Extracting Latent Variables From Forecast Ensembles and Advancements in Similarity Metric Utilizing Optimal Transport. *Journal of Geophysical Research: Machine Learning and Computation* 1. doi:10.1029/2023JH000112.
- Papayiannis, G.I., Galanis, G.N., Yannacopoulos, A.N., 2018. Model aggregation using optimal transport and applications in wind speed forecasting. *Environmetrics* 29. doi:<https://doi.org/10.1002/env.2531>.
- Peyré, G., Cuturi, M., 2019. Computational Optimal Transport: With Applications to Data Science. *Foundations and Trends® in Machine Learning* 11, 355–607. doi:10.1561/22000000073.
- Santambrogio, F., 2015. Optimal Transport for Applied Mathematicians 87. doi:10.1007/978-3-319-20828-2.
- Schmitzer, B., 2019. Stabilized sparse scaling algorithms for entropy regularized transport problems. *SIAM Journal on Scientific Computing* 41, A1443–A1481. doi:10.1137/16M1106018.
- Séjourné, T., Feydy, J., Vialard, F.X., Trouvé, A., Peyré, G., 2019. Sinkhorn Divergences for Unbalanced Optimal Transport URL: <http://arxiv.org/abs/1910.12958>.
- Séjourné, T., Vialard, F.X., Peyré, G., 2022. Faster Unbalanced Optimal Transport: Translation invariant Sinkhorn and 1-D Frank-Wolfe. *Proceedings of Machine Learning Research* 151, 4995–5021. URL: <https://arxiv.org/abs/2201.00730v1>.
- Skok, G., 2022. A New Spatial Distance Metric for Verification of Precipitation. *Applied Sciences* 12. doi:10.3390/app12084048.
- Skok, G., 2023. Precipitation attribution distance. *Atmospheric Research* 295, 106998. doi:10.1016/J.ATMOSRES.2023.106998.
- Skok, G., Lledó, L., 2024. Spatial verification of global precipitation forecasts URL: <https://arxiv.org/abs/2407.20624v1>.
- Vanderbecken, P.J., Dumont Le Brazidec, J., Farchi, A., Bocquet, M., Roustan, Y., Potier, E., Broquet, G., 2023. Accounting for meteorological biases in simulated plumes using smarter metrics. *Atmospheric Measurement Techniques* 16, 1745–1766. doi:10.5194/amt-16-1745-2023.
- Villani, C., 2009. Optimal Transport: Old and New 338. doi:10.1007/978-3-540-71050-9.
- Wernli, H., Paulat, M., Hagen, M., Frei, C., 2008. SAL—A Novel Quality Measure for the Verification of Quantitative Precipitation Forecasts. *Monthly Weather Review* 136, 4470 – 4487. doi:10.1175/2008MWR2415.1.

s

S1 | SUPPLEMENTARY MATERIAL

For full details on optimal transport (OT), its variations, and implementations, consult standard texts such as [Peyré and Cuturi \(2019\)](#); [Villani \(2009\)](#); [Santambrogio \(2015\)](#).

For the unbalanced Sinkhorn updates used in this work, with TV and KL marginal penalisation, see [Séjourné et al. \(2019\)](#) and Section 6 with-in, which defines the log-sum-exp approximation updates used in our implementation ([Francis, n.d.](#)). Their work builds up the unbalanced Sinkhorn divergence derived from the balanced Sinkhorn divergence introduced in [Feydy et al. \(2019\)](#). They provide an overview of the dual-primal relationship that underpins most modern optimal transport theory and applications, however [Peyré and Cuturi \(2019\)](#); [Chizat et al. \(2016\)](#) similarly provide a discrete introduction of this for the balanced and unbalanced setting respectively. It is this dual-primal relationship that enables fast, parallelizable code and offers numerous diagnostic perspectives and tools, all within the same framework.

S1.1 | Specifics of Implementation

Lastly, a brief note on implementation. Code is available at [Francis \(n.d.\)](#). Following [Mérigot and Thibert \(2020\)](#), the mesh, number of Sinkhorn iterates and entropic parameter are linked for balanced OT. In particular, they guarantee error below, $\eta > 0$, given iterations, $k : k \geq e^{\frac{C}{\varepsilon}} \log(\frac{1}{\eta})$ - for some constant C . This remains a heuristic for the unbalanced case, however it appears to work well. In fact, often it is possible to achieve convergence before this, as the theoretical rates are not sharp. Necessarily, ε itself is chosen from the grid resolution, hence it is not user defined; given the average distance realised in the cost function, ε is chosen to keep $e^{-\frac{c(x,y)}{\varepsilon}}$ order 1. In practise then, $\varepsilon \sim 1/\sqrt{N}$, where N is the number of grid points (assuming length scale removed). This similarly defines the expected number of iterations to achieve η convergence, however since convergence is necessary to be able to assign belief in the score more iterations are added to our implementation if this error is not sufficiently low (similarly we may, and often do, terminate early).

Since reaching convergence is essential for this exploration, especially for the realisation of optimal transport vectors, a few different computational techniques and packages are discussed. This should also aid replicability and utility of our findings. Python libraries, such as POT ([Flamary et al., 2021](#)) and GeomLoss ([Feydy et al., 2019](#); [Feydy and Roussillon](#)), are available as off-the-shelf packages. POT provides a wider range of methods; however, GeomLoss has been optimised for machine learning training. GeomLoss does calculate a debiased cost too, though it does not prioritise convergence and instead relies on heuristics to provide an approximately optimal solution suitable for backpropagation and gradient descent. POT, on the other hand, can take into account convergence and provides a range of methods in the unbalanced regime. However, to our knowledge, it does not provide access to the debiased unbalanced Sinkhorn divergence.

Following GeomLoss, our own implementation relies on PyKEOps ([Charlier et al., 2021](#); [Charlier et al.](#)) for fast on-the-fly reductions (suitable for GPUs), while simultaneously taking into account convergence and providing the post-debiasing necessary for forming the Sinkhorn divergence. Since efficiency was not the main goal of this work, rather demonstrating the capacity behind the method, not all possible numerical tricks were employed. In fact, there is an abundance of well-studied tricks, particularly for the balanced OT cases, which may further be used heuristically in the unbalanced case. Such efficiency tricks include ε -scaling, multiscale damping, and kernel truncation ([Schmitzer, 2019](#)), capacity-constrained OT ([Benamou and Martinet, 2020](#)), and more recently, a method known as fast translation-invariant Sinkhorn which is specifically for UOT ([Séjourné et al., 2022](#)).

In this work, two straightforward efficiency methods were employed: ε -scaling, which solves a sequence of problems by progressively reducing ε in multiplicative steps (without fine-to-coarse gaining), and tensorisation for separable cost functions. Additionally, the Python package PyKeOps was utilised for on-the-fly computation, leveraging either CPU or GPU compute.

S1.1.1 | Tensorisation and epsilon-annealing

First, tensorisation relied on the separation of the exponential of the cost function given regular Cartesian coordinates. Note this exponential is known as the kernel and is used in the Sinkhorn algorithm (See Remark 4.17 in [Peyré and Cuturi \(2019\)](#)). Given two regular Cartesian grids, (x_1, x_2) , (y_1, y_2) , and the square Euclidean distance one can write;

$$e^{\frac{(x_{1,i}-y_{1,j})^2+(x_{2,i}-y_{2,j})^2}{2\varepsilon}} = e^{\frac{(x_{1,i}-y_{1,j})^2}{2\varepsilon}} \cdot e^{\frac{(x_{2,i}-y_{2,j})^2}{2\varepsilon}}. \quad (S1)$$

Since the grid is regular $x_{1,i} \in \{x_{1,k}\}_{k=1}^{N_1}$, $x_{2,i} \in \{x_{2,j}\}_{j=1}^{N_2}$, and similarly for $y_{1,j} \in \{y_{1,s}\}_{s=1}^{M_1}$, $y_{2,j} \in \{y_{2,r}\}_{r=1}^{M_2}$, where $N = N_1 \cdot N_2$, $M = M_1 \cdot M_2$. This allows us to reduce the computation memory and only store these smaller matrices,

where any summation can be performed via;

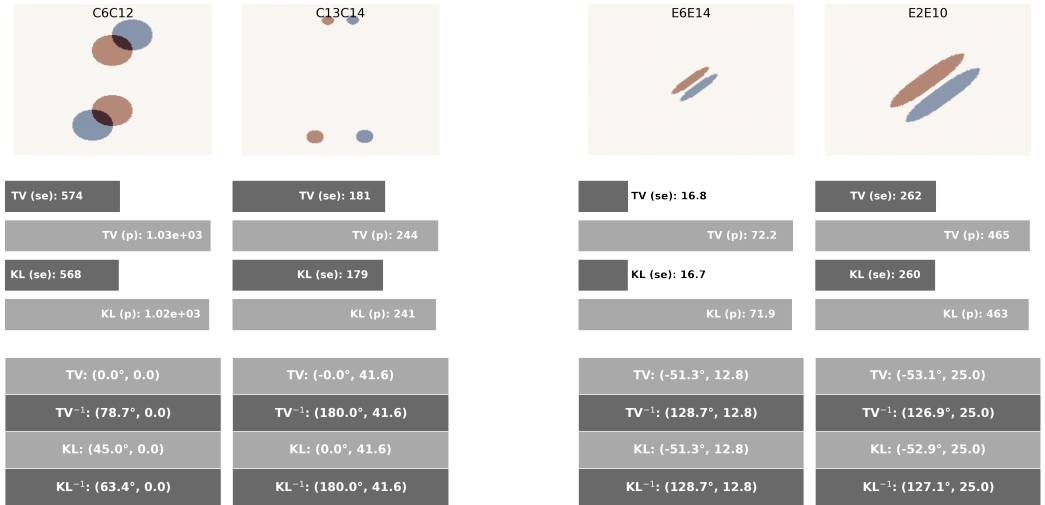
$$\sum_{j=1}^N e^{\frac{c_{i,j}}{\varepsilon}} = \sum_{k=1}^{N_1} e^{\frac{(x_{1,k}-y_{1,j})^2}{2\varepsilon}} \cdot \sum_{l=1}^{N_2} e^{\frac{(x_{2,l}-y_{2,j})^2}{2\varepsilon}} \quad (S2)$$

which reduces the complexity from $O(N)$ to $O(\max(N_1, N_2)) \sim O(\sqrt{N})$.

The second trick, relies on the convexity of the regularisation and that through improved convexity faster convergence in Sinkhorn is realised. By then stepping down in subsequent orders of ε but recycling the potentials from the higher values of ε , a more stable and provably convergent algorithm can be found (Schmitzer, 2019; Chizat, 2024). That is given a value you ε a sequence of problems is solved for $\varepsilon_j \in \{1 \cdot \omega, \dots, \omega^p, \varepsilon\}$ where $\omega < 1$ is some scaling parameter, and $p \in \mathbb{Z}$ such that $\omega^{p+1} \leq \varepsilon$. Previous optimal solutions are used as an initialisation to the subsequent one.

S1.2 | Extra Figures

Fig. S1a illustrates two cases where multiple features are present in both fields, each exhibiting some form of symmetry. Case C6C12 shows the expected cost given the known total translation; however, the ATM cancels out because the translations are equal and opposite. Case C13C14 also shows the expected cost given the known translational error. Here, the ATM is an appropriately scaled version of the total transport, as the northern two features are mapped to each other, and similarly, the southern two features are mapped to each other. Fig. S2 shows this behaviour by viewing the transport vectors, clearly demonstrating that these distinct features remain separate in the transport.



(a) Balanced multiple features case, demonstrating that the logic of transportation holds when two transported features are present

(b) Balanced cases, yet with scaled size of events. The S_ε and ATM together allow powerful diagnostics of ranking, direction, and magnitude.

FIGURE S1 Figures exploring multiple features and scaling between different sizes of events. The top four horizontal bars display; $S_\varepsilon^{TV}, UOT_\varepsilon^{TV}, S_\varepsilon^{KL}, UOT_\varepsilon^{KL}$. The lower table presents the mean (ATD, ATM) in both flavours, and with the forward and inverse vectors. The red (darker) colour indicates observations, while the blue (lighter) represents forecasts. $\varepsilon = 0.005 \cdot L^2, \rho = 1 \cdot L^2$.

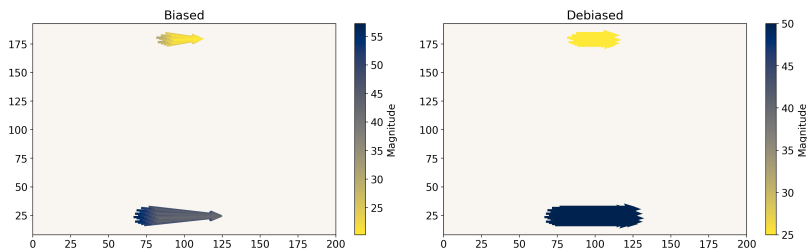


FIGURE S2 Biased vs debiased transport vector illustration with TV marginal penalty for the C13C14 case. Note, in the approximate map, the supports are still retained due to entropic regularisation, which assigns some mass to the supports and is defined everywhere by extension to the convex hull. Left: Biased UOT transport vectors, Right: Debiased UOT transport vectors. A regular sample of the vectors are shown to prevent overcrowding. $\varepsilon = 0.005 \cdot L^2$, $\rho = 2^{-4} \cdot L^2$.

Fig. S1b compares cases E6E14 and E2E10. Firstly, the debiased cost in both flavours correctly identifies the translational error. This is also reflected in the ATD and ATM. Secondly, they demonstrate that the cost is capable of scaling directly with the size of the event, i.e., the ellipses in E2 and E10 are 4 times larger, and there is approximately twice the transport. Then $16.8 \cdot 4 \cdot 2^2 \sim 269$.

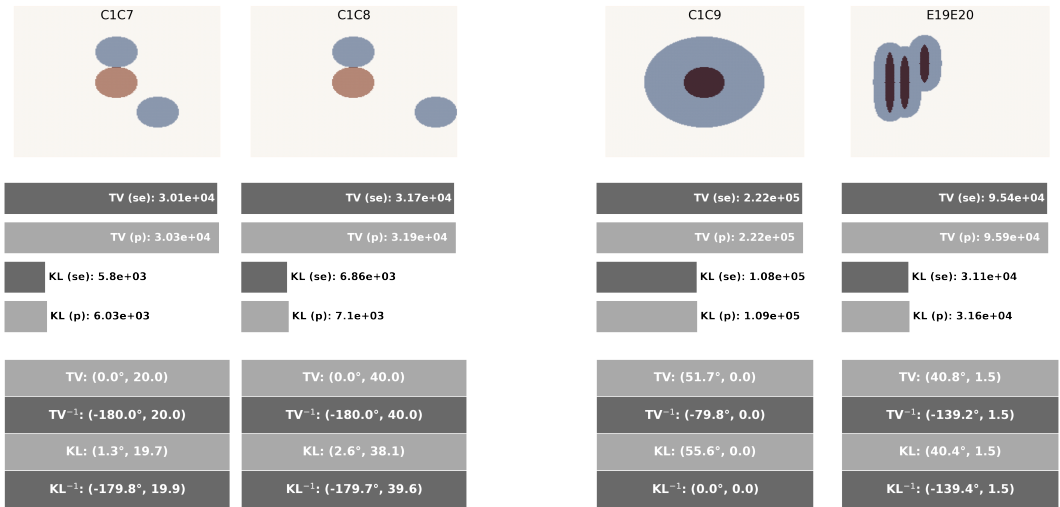
Fig. S3a explore the unbalanced setting ρ dependence. These combine with C1C6, and Fig. S4a, Fig. S4b which illustrate the returned marginals. Notably, the strict reach interpretation is now ruined in this very unbalanced setting. Instead, for the symmetric cases C1C6 the reach appears to have a halved influence, though when this symmetry is destroyed, mass is assigned to the closer feature. Moreover, the costing between KL and TV is now very different. Here TV penalises the large mass imbalanced very harshly. The ATD and ATM then are suffering from a mean averaging downfall — they average out in the north-south shifts, and diagnoses only the west-east shift. This is a known issue and could be overcome by viewing the whole spread of vectors direction and magnitude.

Fig. S3b establishes UOT's behaviour when an event is a subset of another. Crucially, these are highly imbalanced cases and largely penalised for this large imbalanced. Moreover, this alone does not allow for diagnosis of an event being a subset of another. The cost alone does not provide this information. One potential route is through the 2D histogram of the transport vectors magnitude and directions; Fig. S5, Fig. S6 & Fig. S7. Observe for the simple cases C1C9 that the spread is uniform across a full 360° , however for the non-symmetric case E19E20 this uniform spread is lost. However, this is still a spread across all angles. This is a necessary but not sufficient condition of subset diagnosis. i.e. one could construct a case where the transport covers all angles but is not a subset of the other — C1C10 (Fig. S15) is in case such a case.

For a better understanding of how UOT does treat rotation, consider Fig. S8 & Fig. S9, which illustrates the transport vectors for rotated objects E2E4 under Tv and KL marginal penalisation respectively. Observe that the transport vectors squeeze and stretch the shape, not rotate. Instead, this follows an aspect-ratio correction, rather than rotation.

S1.2.1 | Real textured cases

Fig. S10 demonstrates the returned cost for the perturbed fake cases, now with a small reach parameter. This means that the transport is kept more local. This has the effect that TV is able to diagnose more reasonably to the expected score, though KL still performed better in this imbalanced setting. Additionally, both improve their ATM and ATD since only local transport is allowed. However, in the more perturbed cases, which now go above the reach, the ATD and ATM struggle to align with the expected displacement: 5.8, approximately doubling sequentially (11.7, 23.3, 46.6, 93.3), and in the forward direction at a maintained -59° . However, in Fig. S11 & Fig. S12, the ATM and ATD are restored,



(a) Illustration of cases C1C7, and C1C8, where there are two events, but the lower event moves away and thus becomes less associated with the closest event.

(b) Testing UOT with subset events. The S_ϵ and ATM together allow powerful diagnostics of ranking, direction, and magnitude.

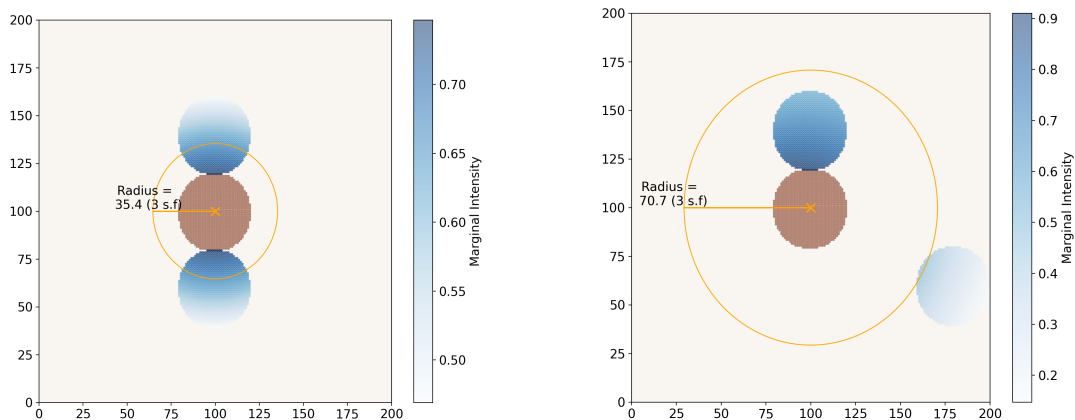
FIGURE S3 Figures exploring multiple features and if UOT can diagnose subsetted events. The top four horizontal bars display; S_ϵ^{TV} , UOT_ϵ^{TV} , S_ϵ^{KL} , UOT_ϵ^{KL} . The lower table presents the mean (ATD, ATM) in both flavours, and with the forward and inverse vectors. The red (darker) colour indicates observations, while the blue (lighter) represents forecasts. $\epsilon = 0.005 \cdot L^2$, $\rho = 1 \cdot L^2$.

closer to the expected values, simply by changing the averaging from a mean average to the median.

Fig. S13 shows ATM data to pair with Fig. 14. Observe the same anomalies for found on May 25th and May 19th. Then Fig. S14 illustrates the transport vectors with KL marginal penalisation, found on May25th between the observations ST2ml_2005052500.g240 (blues shades) and forecast wrf4ncar_2005052400.g240.f24 (orange shades). notice the events that are well-matched; those in the north-west corner and those around Arkansas. However, within the forecast there is a large missing feature above Nebraska and on the Mexico boarder. This in turns has lead to large transport required to correct the missing features, and it is found in the forward and inverse map.

S1.3 | Missing cases

To avoid cherry-picking results the full array of testing cases are presented to align with Gilleland et al. (2020). Together with the results above all cases included in the initial study are repeated here for UOT in two flavours. The top four horizontal bars display; S_ϵ^{TV} , UOT_ϵ^{TV} , S_ϵ^{KL} , UOT_ϵ^{KL} . The lower table presents the mean (ATD, ATM) in both flavours, and with the forward and inverse vectors. The red (darker) colour indicates observations, while the blue (lighter) represents forecasts. $\epsilon = 0.005 \cdot L^2$, $\rho = 1 \cdot L^2$.



(a) Case C1C6 with KL marginal penalty. The marginal π_1 shows again there is a strict relationship to the reach parameter, although the mass is shared within half the reach. Hence, the radius shown is equal to half reach.

$$\varepsilon = 0.005 \cdot L^2, \rho = 2^{-4} \cdot L^2.$$

(b) Case C1C8 with KL marginal penalty. The marginal π_1 shows again there is no longer a strict relationship to the reach parameter, and mass is assigned to the closer feature. The radius shown is equal to the reach.

$$\varepsilon = 0.005 \cdot L^2, \rho = 2^{-4} \cdot L^2.$$

FIGURE S4 Comparison of cases C1C6 and C1C8 with KL marginal penalty.

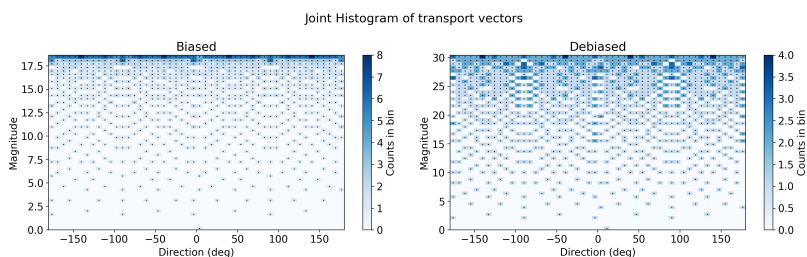


FIGURE S5 2D histogram of the magnitude and direction of the underlying transports vectors for the perturbed case C1C9 which has a full 360° of necessary transport since one event is a subset of the other. The dotted bins, indicate those with non-zero mass. These results are based on TV marginal penalisation with parameters $\varepsilon = 0.001 \cdot L^2, \rho = L^2$

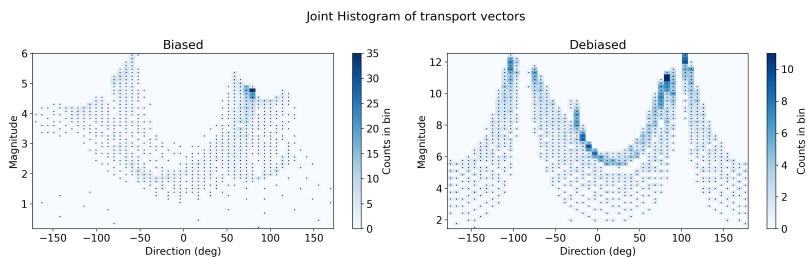


FIGURE S6 2D histogram of the magnitude and direction of the underlying transports vectors for the perturbed case E19E20 which has a full 360° of necessary transport since one event is a subset of the other. The dotted bins, indicate those with non-zero mass. These results are based on KL marginal penalisation with parameters $\varepsilon = 0.001 \cdot L^2, \rho = L^2$

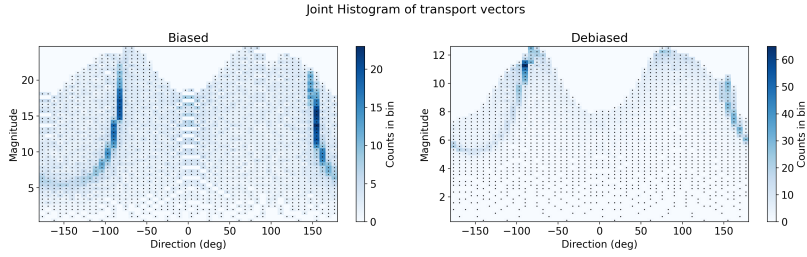


FIGURE S7 2D histogram of the magnitude and direction of the underlying transports vectors for the perturbed case E20E19 (reverse of S6) which has a full 360° of necessary transport since one event is a subset of the other. The dotted bins, indicate those with non-zero mass. These results are based on KL marginal penalisation with parameters $\varepsilon = 0.001 \cdot L^2$, $\rho = L^2$

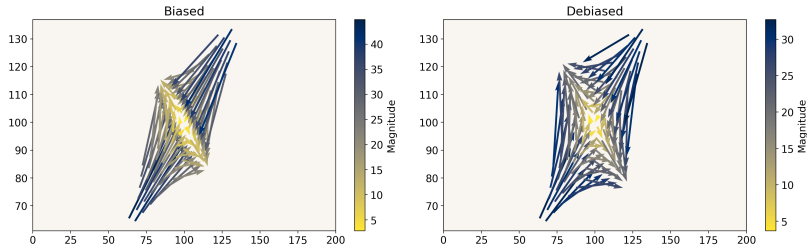


FIGURE S8 Biased vs debiased transport vector illustration with TV marginal penalty for the E2E4 case. Here the squeezing and stretching behaviour for rotated objects is demonstrated. Left: Biased UOT transport vectors, Right: Debiased UOT transport vectors. A regular sample of the vectors are shown to prevent overcrowding. $\varepsilon = 0.005 \cdot L^2$, $\rho = 1 \cdot L^2$.

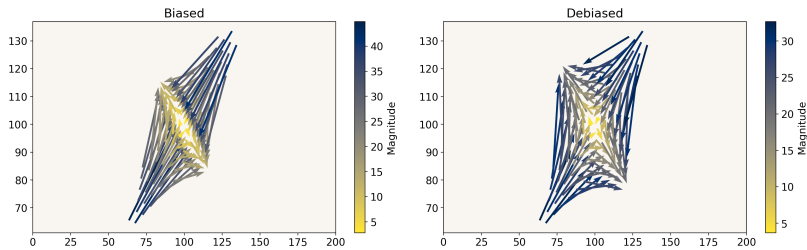


FIGURE S9 Biased vs debiased transport vector illustration with KL marginal penalty for the E2E4 case. Here the squeezing and stretching behaviour for rotated objects is demonstrated. Left: Biased UOT transport vectors, Right: Debiased UOT transport vectors. A regular sample of the vectors are shown to prevent overcrowding. $\varepsilon = 0.005 \cdot L^2$, $\rho = 1 \cdot L^2$.

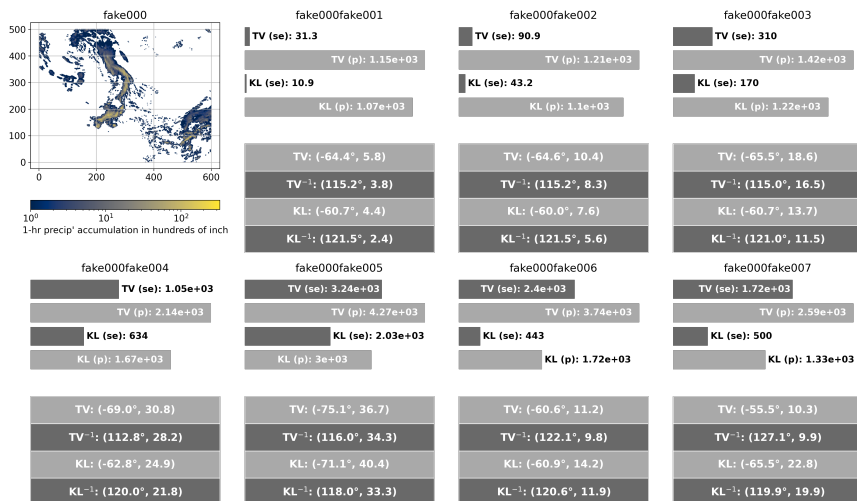


FIGURE S10 Perturbed cases with real textured intensities. All cases are a changed version of fake000, shown in the top left. The top four horizontal bars display; S_{ε}^{TV} , UOT_{ε}^{TV} , S_{ε}^{KL} , UOT_{ε}^{KL} . The lower table presents the mean (ATD, ATM) in both flavours, and with the forward and inverse vectors. The red (darker) colour indicates observations, while the blue (lighter) represents forecasts. $\varepsilon = 0.001$, $\rho = 2^{-6} \cdot L^2$, reach ~ 106 .

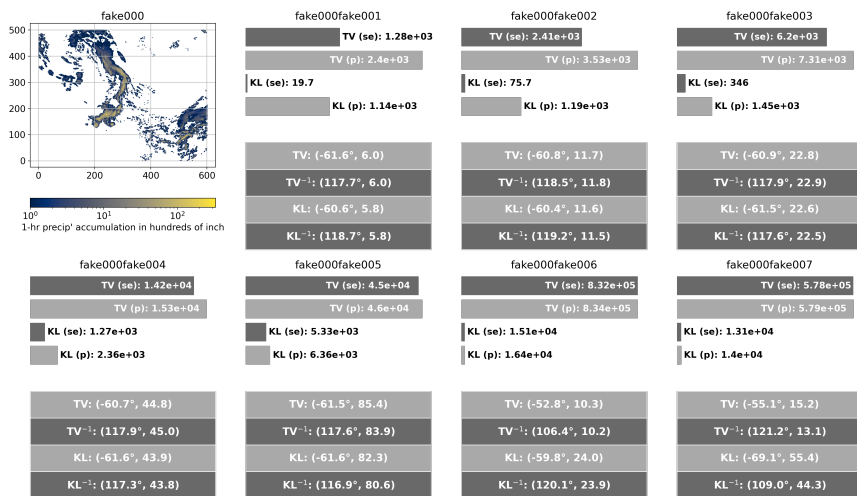


FIGURE S11 Median ATM version of 12. The top four horizontal bars display; S_{ε}^{TV} , UOT_{ε}^{TV} , S_{ε}^{KL} , UOT_{ε}^{KL} . The lower table presents the median ATM and ATD in both flavours, and with the forward and inverse vectors. The red (darker) colour indicates observations, while the blue (lighter) represents forecasts. $\varepsilon = 0.001$, $\rho = 2^{-6} \cdot L^2$, reach ~ 106 .

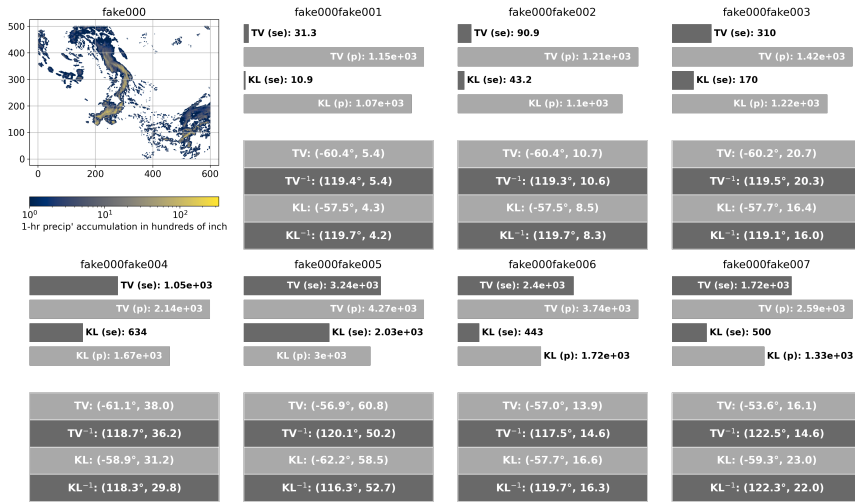


FIGURE S12 Median ATM version of S10. The top four horizontal bars display; S_{ϵ}^{TV} , UOT_{ϵ}^{TV} , S_{ϵ}^{KL} , UOT_{ϵ}^{KL} . The lower table presents the median ATM and ATD in both flavours, and with the forward and inverse vectors. The red (darker) colour indicates observations, while the blue (lighter) represents forecasts. $\epsilon = 0.001, \rho = 2^{-6} \cdot L^2$, reach ~ 106 .

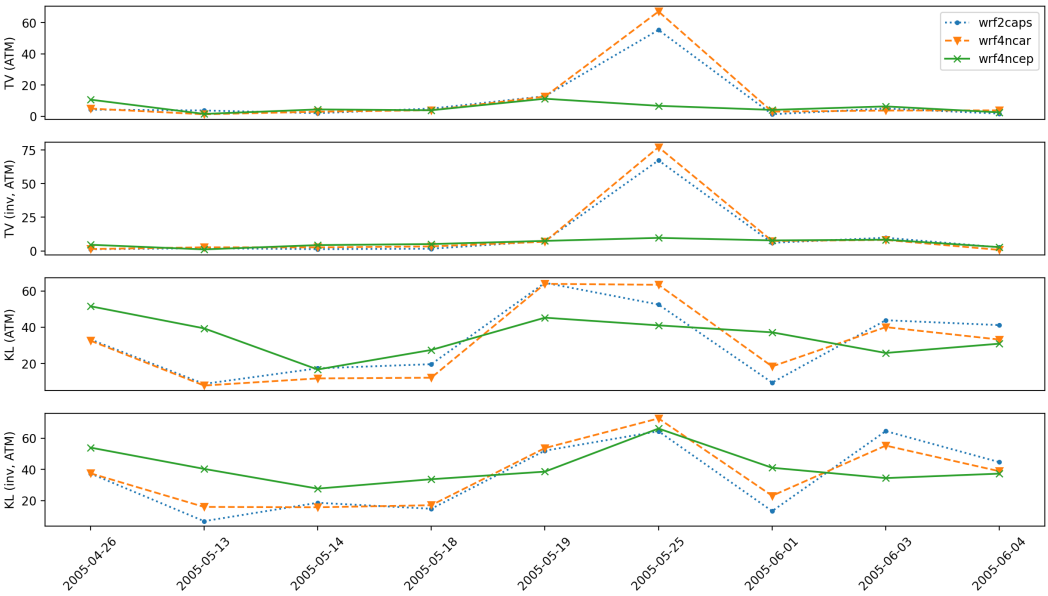


FIGURE S13 Spring 2005 cases with 9 times stamps, demonstrating the ATM and inverse (inv) ATM shown across flavours and time. There is again a clear anomaly on 2005-05-25 in both flavours, and an anomaly on the 2005-05-19 in the KL penalty. Each model was at 24hr lead time, and interpolated on the coarser 4km grid. $\epsilon = 0.001 \cdot L^2, \rho = L^2$.

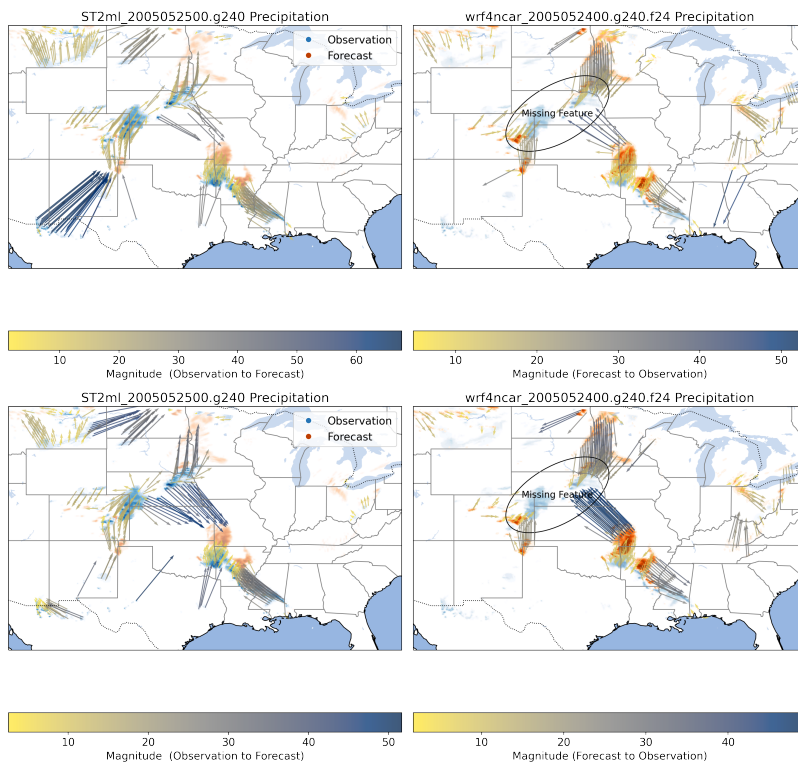


FIGURE S14 Illustration of the transport vectors with KL (Top rows) and TV (bottom rows) marginal penalisation, found on May25th between the observations ST2ml_2005052500.g240 (blues shades) and forecast wrf4ncar_2005052400.g240.f24 (orange shades). Notice the events that are well-matched; those in the north-west corner and those around Arkansas. There is a large missing feature above Nebraska in the forecast, which is contained in the ellipse (RHS). Left: Observation to forecast transport vectors with forecast intensities superimposed in lighter shades, Right: Forecast to observation transport vectors with observation intensities superimposed in lighter shades. $\varepsilon = 0.001 \cdot L^2, \rho = 2^{-6} \cdot L^2$

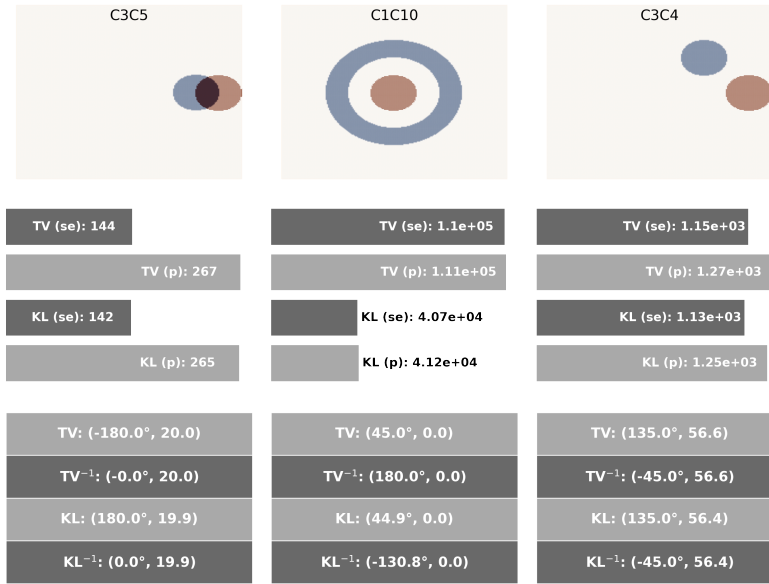


FIGURE S15 Cases C3C5, C1C10, C3C4. C3C5, C3C4 are pairs with C1C4, and C2C5 since they are reflected to shifted versions (relative to the boundary). C1C10 confirms the necessary but not sufficient condition of finding subsets of events, since the transport required here has a similar spread to C1C9 yet, C1 is not contained within C10. The top four horizontal bars display; S_{ε}^{TV} , UOT_{ε}^{TV} , S_{ε}^{KL} , UOT_{ε}^{KL} . The lower table presents the mean (ATD, ATM) in both flavours, and with the forward and inverse vectors. The red (darker) colour indicates observations, while the blue (lighter) represents forecasts. $\varepsilon = 0.005 \cdot L^2$, $\rho = 1 \cdot L^2$

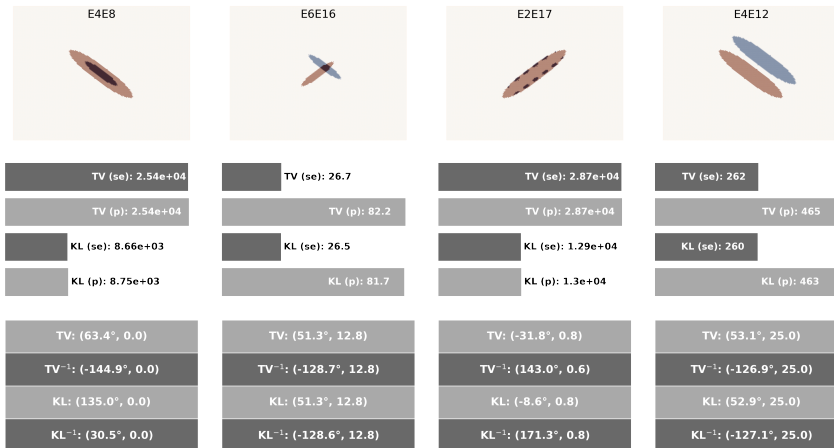


FIGURE S16 Cases E4E8, E6E16, E2E17, E4E12, which demonstrate different behaviours on scales, scatter showers in an envelope and simple transportation. All are considered more realistic shapes for complex terrain than the circular cases. The top four horizontal bars display; S_{ε}^{TV} , UOT_{ε}^{TV} , S_{ε}^{KL} , UOT_{ε}^{KL} . The lower table presents the mean (ATD, ATM) in both flavours, and with the forward and inverse vectors. The red (darker) colour indicates observations, while the blue (lighter) represents forecasts. $\varepsilon = 0.005 \cdot L^2$, $\rho = 1 \cdot L^2$

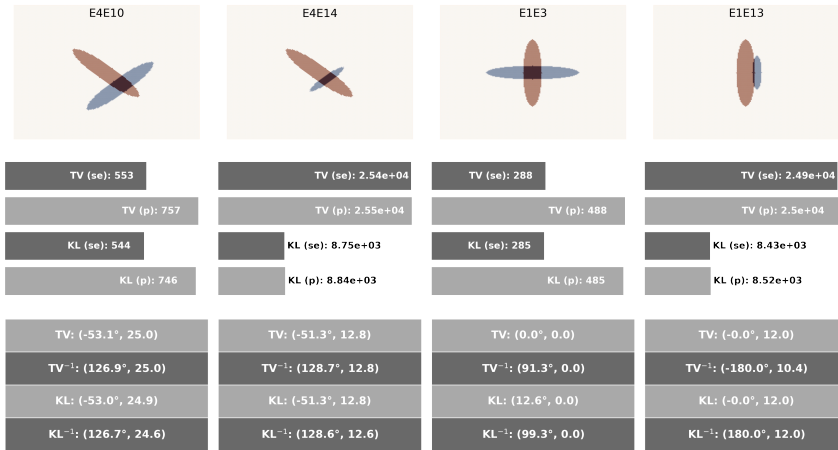


FIGURE S17 Cases E4E10, E4E14, E1E3, E1E13, which demonstrate different behaviours on scales, rotation, or aspect ratio errors and combinations of both. All are considered more realistic shapes for complex terrain than the circular cases. The top four horizontal bars display; S_{ϵ}^{TV} , UOT_{ϵ}^{TV} , S_{ϵ}^{KL} , UOT_{ϵ}^{KL} . The lower table presents the mean (ATD, ATM) in both flavours, and with the forward and inverse vectors. The red (darker) colour indicates observations, while the blue (lighter) represents forecasts. $\epsilon = 0.005 \cdot L^2$, $\rho = 1 \cdot L^2$



FIGURE S18 Cases E5E7, E2E18, E2E6, E1E11, which demonstrate different behaviours on scales, rotation with translation as well as missed scatter showers. All are considered more realistic shapes for complex terrain than the circular cases. The top four horizontal bars display; S_{ϵ}^{TV} , UOT_{ϵ}^{TV} , S_{ϵ}^{KL} , UOT_{ϵ}^{KL} . The lower table presents the mean (ATD, ATM) in both flavours, and with the forward and inverse vectors. The red (darker) colour indicates observations, while the blue (lighter) represents forecasts. $\epsilon = 0.005 \cdot L^2$, $\rho = 1 \cdot L^2$

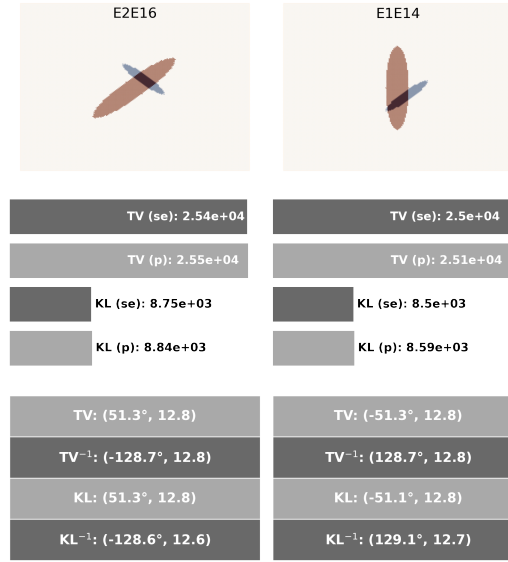


FIGURE S19 Cases E2E16, E1E14, which demonstrate different behaviours with scales rotation and transitional error combined. All are considered more realistic shapes for complex terrain than the circular cases. The top four horizontal bars display; S_{ε}^{TV} , UOT_{ε}^{TV} , S_{ε}^{KL} , UOT_{ε}^{KL} . The lower table presents the mean (ATD, ATM) in both flavours, and with the forward and inverse vectors. The red (darker) colour indicates observations, while the blue (lighter) represents forecasts. $\varepsilon = 0.005 \cdot L^2$, $\rho = 1 \cdot L^2$

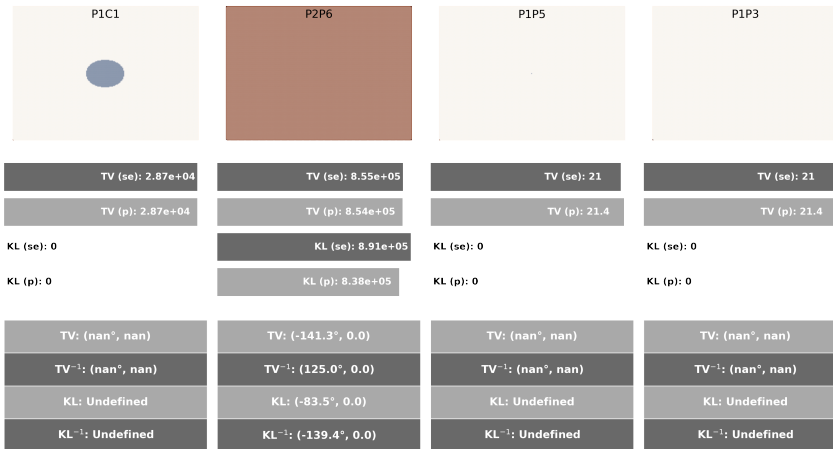


FIGURE S20 Cases P1C1, P2P6, P1P5, P1P3, recall that P1 is the null field, hence some quantities are undefined or zero. P1C1, P1P5, P1P3 KL (se) and KL (p) are defined as zero. The top four horizontal bars display; S_{ε}^{TV} , UOT_{ε}^{TV} , S_{ε}^{KL} , UOT_{ε}^{KL} . The lower table presents the mean (ATD, ATM) in both flavours, and with the forward and inverse vectors. The red (darker) colour indicates observations, while the blue (lighter) represents forecasts. $\varepsilon = 0.005 \cdot L^2$, $\rho = 1 \cdot L^2$

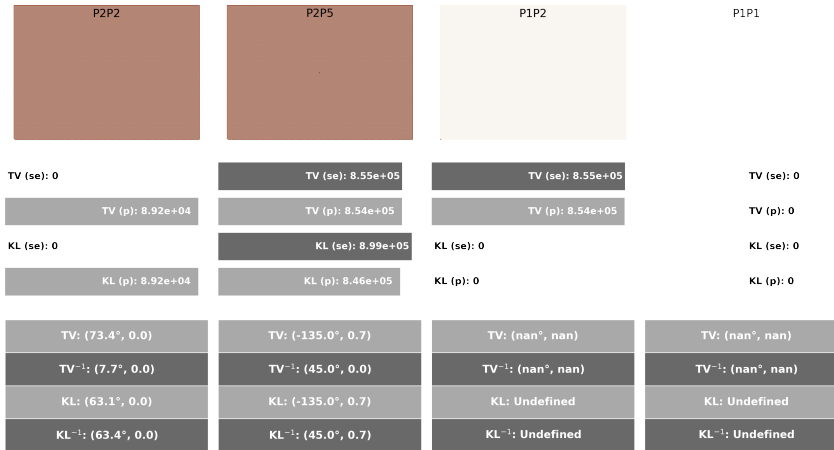


FIGURE S21 Cases P2P2, P2P5, P1P2, P1P1, recall that P1 is the null field, hence some quantities are undefined or zero. P2P2 returns the expected score for a perfect match of zero necessary transport. P1P2, P1P1 KL (se) and KL (p) are defined as zero. The top four horizontal bars display; S_{ε}^{TV} , UOT_{ε}^{TV} , S_{ε}^{KL} , UOT_{ε}^{KL} . The lower table presents the mean (ATD, ATM) in both flavours, and with the forward and inverse vectors. The red (darker) colour indicates observations, while the blue (lighter) represents forecasts. $\varepsilon = 0.005 \cdot L^2$, $\rho = 1 \cdot L^2$

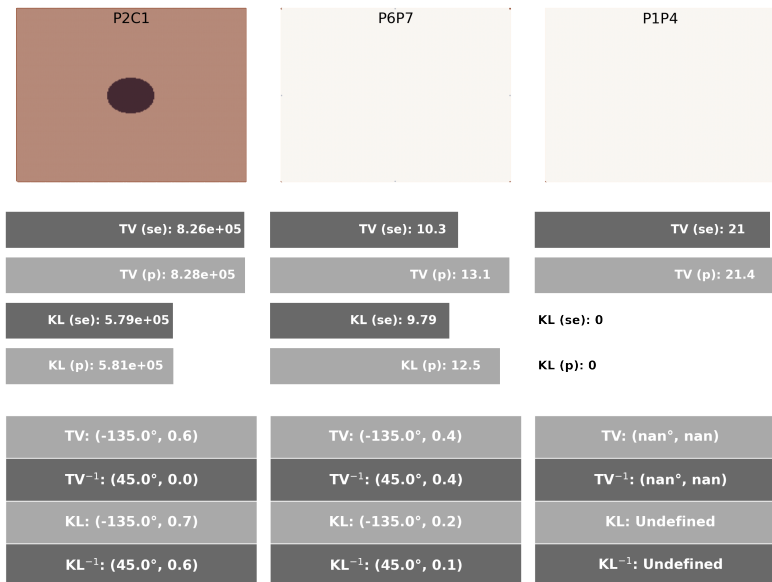


FIGURE S22 Cases P2C1, P6P7, P1P4, recall that P1 is the null field, hence some quantities are undefined or zero. P1P4, KL (se) and KL (p) are defined as zero. The top four horizontal bars display; S_{ε}^{TV} , UOT_{ε}^{TV} , S_{ε}^{KL} , UOT_{ε}^{KL} . The lower table presents the mean (ATD, ATM) in both flavours, and with the forward and inverse vectors. The red (darker) colour indicates observations, while the blue (lighter) represents forecasts. $\varepsilon = 0.005 \cdot L^2$, $\rho = 1 \cdot L^2$